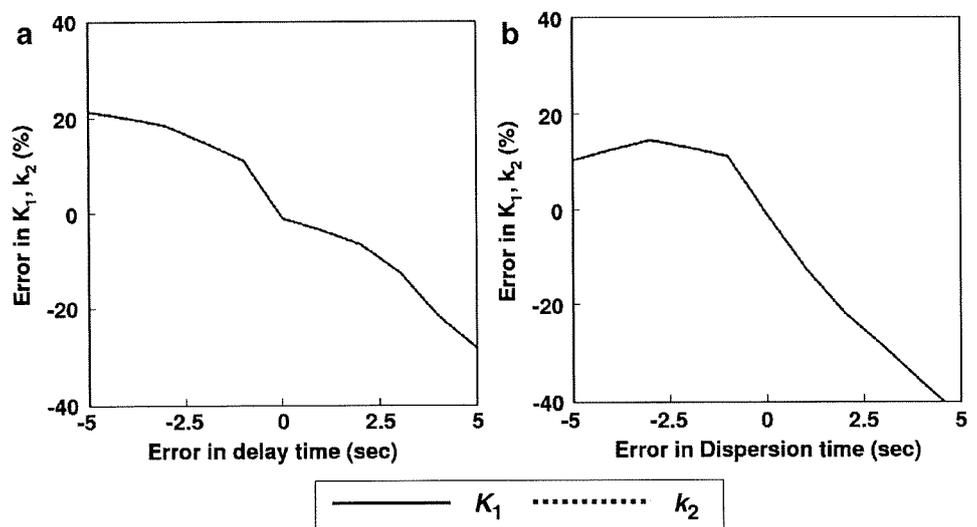**Fig. 5** Error propagation from the error in input time (**a**) and dispersion time constant (**b**) to K_1 and k_2 (the two lines were identical). Positive and negative values of error indicate over- and under-correction of delay time and dispersion time, respectively

estimate the rate constants of K_1 and/or k_2. Also V_A cannot be ignored, even when only relative rate constant values are needed. These findings suggest that the present k_2 obtained BFM technique provides an RBF image with reasonable accuracy and quality.

In the present study the rate constants of K_1 and k_2 were experimentally computed, and the ratios obtained ranged from 0.35 to 0.45 ml/g, which corresponds to the apparent kidney–blood partition coefficient. The much smaller apparent p value might be due to a partial volume effect, as has been demonstrated in a previous brain and cardiac study [10, 11], because of the composite structure of the kidney, the spatial resolution of the reconstructed image and breathing movement of the patient during the scan. When the rate constant K_1 is underestimated due to the partial

Fig. 6 Error propagation from the partition coefficient (p, ml/g) to K_1 and k_2. When the true p was varied between 0.6 and 0.8 ml/g, the size of the error in RBF was simulated assuming p=0.7 ml/g

volume effect, $k_2 \cdot p_{phys}$ could be applied for RBF rather than K_1. The present study showed that the contribution of GFR to the clearance rate was only 10%, and that $k_2 \cdot p_{phys}$ is more appropriate for RBF assessment, although further study of how the GFR changes under stimulated conditions is required. The $k_2 \cdot p_{phys}$ value in the cortical region obtained in the present study was 3.64±2.15 ml/min/g under normal condition, a value within the normal range of 4 to 5 ml/min/g reported in the literature [22]. Middlekauff et al. [23–25] applied the ROI base analysis, and showed similar RBF values around 4 ml/min/g. These findings also support the use of $k_2 \cdot p_{phys}$ for the calculation of RBF. The different values of RBF between the present study and the previous studies [3–5] might be due to differences in the approaches.

The present computation of RBF by the BFM has two main advantages over the NLF. One is the ability to produce a voxel-by-voxel quantitative parametric map, and the other is faster computing speed. In fact, the parametric images were obtained within a reasonable time, i.e. 2.5 min with an image size of 128×128 pixels with 35 slices and 22 frames. The time could be further reduced by applying a threshold to omit pixels with lower values. From a clinical standpoint, voxel-by-voxel analysis is preferred to ROI-based analysis because the operator can independently define ROIs to improve reproducibility, and faster computations are important for analysing very large datasets.

Kinetic parameters estimated by the NLF agreed well with those estimated by the BFM as shown in Fig. 2. The disagreement in some rate constant values between the voxel-based (BFM) and ROI-based computation methods might have been due to the composite structure between the cortical region and its surroundings, or to image noise. Although superior to the NLF in terms of computing speed and ability to generate parametric maps, the BFM shares the same source of errors as the NLF because they use the
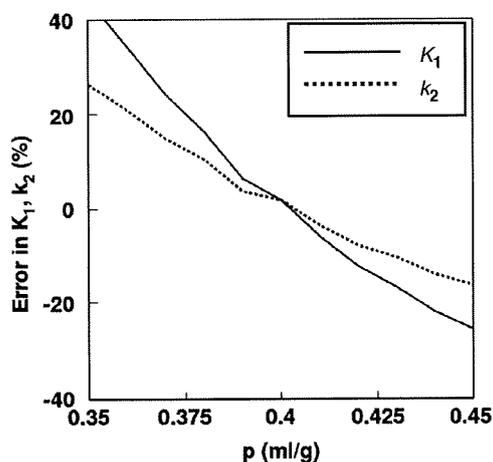
Fig. 7 a Error propagation from the arterial blood volume (V_A, ml/ml) to K_1 and k_2 (the two lines were identical). When the true V_A changed from 0.0 to 0.4 ml/ml, the size of the error in K_1 and k_2 calculated assuming V_A=0.0 ml/ml was simulated. **b** Error propagation from the change in arterial blood volume from 0.14 ml/ml (ΔV_A) to the change in K_1 and k_2 from the initial conditions (ΔK_1 and Δk_2, ml/min/g) (the two lines were identical)
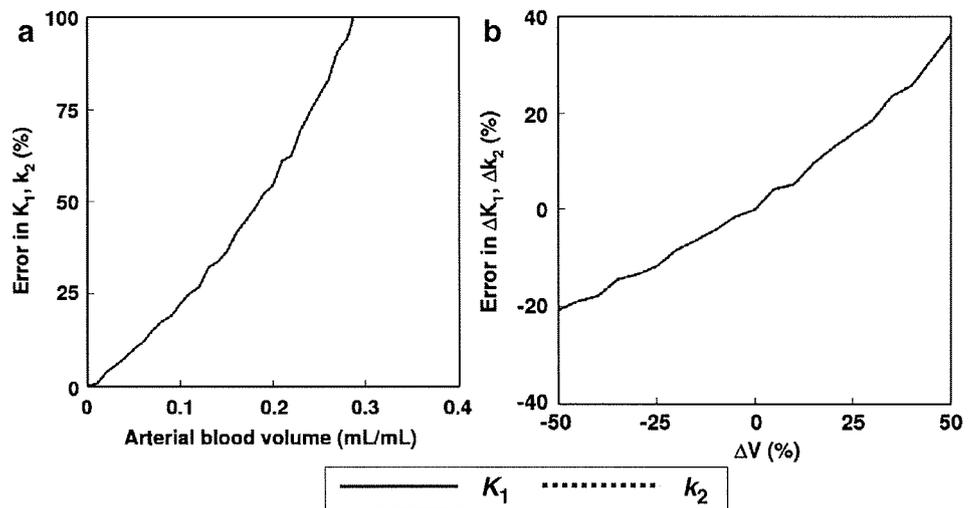
same model and assumption. Delay and dispersion in input function, motion of the patient during a study [26–28], and flow heterogeneity [29] are sources of error for parameters estimated by both the NLF and BFM. Selection of a specific range of k_2 and the number of basis function can affect the accuracy and precision of the estimated parameters in neuroreceptor studies [30, 31]. However, the range was 0 to 15 ml/min/g in the present computation with $H_2^{15}O$, and the limits of this range would be acceptable for the present computation. In practice, selection of a wider range and/or a large number of discrete values of the basis function is slow and inefficient against the required accuracy and precision.

The present simulation study showed that if V_A is neglected or fixed, not only the absolute rate constants, i. e. RBF value, are overestimated, but estimated changes in RBF between two physiological states could be over- or underestimated. These findings suggest that V_A should be included to obtain either absolute or relative values of RBF. For p, the present simulation revealed that the error sensitivity in RBF for that value was significant. The values of p for the whole and cortical regions were 0.35 and 0.42 ml/g, respectively. If the value was fixed at 0.4 ml/g, a 40% overestimation in RBF for regions with a p of 0.35 occurred. Thus, regional difference in p introduce error in quantitative RBF values. Also the AIC analysis showed that introducing the extra parameters of p and V_A did not increase the AIC value against the others. These findings suggest that both p and V_A need to be estimated simultaneously with quantitative RBF, especially when changes under different conditions are assessed.

Knowledge of RBF is mostly needed in determining the severity of renovascular disease. Although the degree of renal artery stenosis is easily diagnosed, its actual effect on RBF remains difficult to quantify. In clinical work,

estimates of GFR have not shown very good accuracy in relation to possible interventional treatment. Also, there is no good clinical method to easily measure single-kidney or regional RBF. We can obtain the effective renal plasma flow (ERPF) by infusing p-aminohippuric acid and measuring the urine and plasma concentrations, but this method only gives the total ERPF for both kidneys. An alternative is a magnetic resonance (MR) based method, which is problematic in patients with chronic kidney disease, because the contrast agent gadolinium is contraindicated in these subjects [32]. The present PET-related methodology may provide quantitative estimate of regional RBF, and be clinically applicable under conditions such as chronic allograft nephropathy and acute kidney insufficiency. The procedure – as presented here – still involves a small degree of invasiveness because of blood sampling. However, many noninvasive methods for estimating input functions have been proposed [3–5, 23–25, 33, 34], and their implementation will allow RBF to be determined in a fully noninvasive fashion, particularly for clinical purposes.

In conclusion, although some issues remain to be investigated, this study shows the feasibility of measurement of RBF using PET with $H_2^{15}O$.

Springer

References

1. Nitzsche EU, Choi Y, Killion D, Hoh CK, Hawkins RA, Rosenthal JT, et al. Quantification and parametric imaging of renal cortical blood flow in vivo based on Patlak graphical analysis. Kidney Int 1993;44:985–96.
2. Szabo Z, Xia J, Mathews WB, Brown PR. Future direction of renal positron emission tomography. Semin Nucl Med 2006;36:36–50.
3. Juillard L, Janier MF, Foucue D, Lionnet M, Le Bars D, Cinotti L, et al. Renal blood flow measurement by positron emission tomography using 15O-labeled water. Kidney Int 2000;57:2511–18.
4. Juillard L, Janier MF, Fouque D, Cinotti L, Maakel N, Le Bars D, et al. Dynamic renal blood flow measurement by positron emission tomography in patients with CRF. Am J Kidney Dis 2002;40:947–54.
5. Alpert NM, Rabito CA, Correia DJA, Babich JW, Littman BH, Tompkins RG, et al. Mapping of local renal blood flow with PET and H2 15O. J Nucl Med 2002;43:470–75.
6. Anderson HL, Yap JT, Miller MP, Robbins A, Jones T, Price PM. Assessment of pharmacodynamic vascular response in a phase I trial of combretastatin A4 phosphate. J Clin Oncol 2003;21:2823–30.
7. Anderson H, Yap JT, Wells P, Miller MP, Propper D, Price D, et al. Measurement of renal tumour and normal tissue perfusion using positron emission tomography in a phase II clinical trial of razoxane. Br J Cancer 2003;89:262–67.
8. Snyder WS, Cook MJ, Nasset ES, Karhausen LR, Howells GP, Tipton IH. Report of the Task Group on Reference Man. London: Pergamon Press; 1974. p. 175–77.
9. Herscovitch P, Raichle ME. What is the correct value for the brain–blood partition coefficient for water? J Cereb Blood Flow Metab 1985;5:65–9.
10. Iida H, Law I, Pakkenberg B, Krarup-Hansen A, Eberl S, Holm S, et al. Quantitation of regional cerebral blood flow corrected for partial volume effect using O-15 water and PET: I. Theory, error analysis, and stereologic comparison. J Cereb Blood Flow Metab 2000;20:1237–51.
11. Blomqvist G, Lammertsma AA, Mazoyer B, Wienhard K. Effect of tissue heterogeneity on quantification in positron emission tomography. Eur J Nucl Med 1995;22:652–63.
12. Koeppe RA, Holden JE, Ip WR. Performance comparison of parameter estimation techniques for the quantitation of local cerebral blood flow by dynamic positron computed tomography. J Cereb Blood Flow Metab 1985;5:224–34.
13. Gunn RN, Lammertsma AA, Hume SP, Cunningham VJ. Parametric imaging of ligand-receptor binding in PET using a simplified reference region model. Neuroimage 1997;6:279–87.
14. Watabe H, Jino H, Kawachi N, Teramoto N, Hayashi T, Ohta Y, et al. Parametric imaging of myocardial blood flow with 15O-water and PET using the basis function method. J Nucl Med 2005;46:1219–24.
15. Boellaard R, Knaapen P, Rijbroek A, Luurtsema GJ, Lammertsma AA. Evaluation of basis function and linear least squares methods for generating parametric blood flow images using 15O-water and positron emission tomography. Mol Imaging Biol 2005;7:273–85.
16. Ruotsalainen U, Raitakari M, Nuutila P, Oikonen V, Sipilä H, Teräs M, et al. Quantitative blood flow measurement of skeletal muscle using oxygen-15-water and PET. J Nucl Med 1997;38:314–19.
17. Levey A, Bosch J, Lewis J, Greene T, Rogers N, Roth D. A more accurate method to estimate glomerular filtration rate from serum creatinine: a new prediction equation. Modification of Diet in Renal Disease Study Group. Ann Intern Med 1999;130:461–70.
18. Iida H, Kanno I, Miura S, Murakami M, Takahashi K, Uemura K. Error analysis of a quantitative cerebral blood flow measurement using H2 15O autoradiography and positron emission tomography, with respect to the dispersion of the input function. J Cereb Blood Flow Metab 1986;6:536–45.
19. Iida H, Higano S, Tomura N, Shishido F, Kanno I, Miura S, et al. Evaluation of regional differences of tracer appearance time in cerebral tissues using [15O] water and dynamic positron emission tomography. J Cereb Blood Flow Metab 1988;8:285–88.
20. Akaike H. A new look at the statistical model identification. IEEE Trans Automat Contr 1974;AC19:716–23.
21. Kudomi N, Hayashi T, Teramoto N, Watabe H, Kawachi N, Ohta Y, et al. Rapid quantitative measurement of CMRO2 and CBF by dual administration of 15O-labeled oxygen and water during a single PET scan – a validation study and error analysis in anesthetized monkeys. J Cereb Blood Flow Metab 2005;259:1209–24.
22. Ganong WF. Review of medical physiology. 8th ed. Norwalk: Appleton & Lange; 1977. p. 522–45.
23. Middlekauff HR, Nitzsche EU, Hamilton MA, Schelbert HR, Fonarow GC, Moriguchi JD, et al. Evidence for preserved cardiopulmonary baroflex control of renal cortical blood flow in humans with advanced heart failure. Circulation 1995;92:395–401.
24. Middlekauff HR, Nitzsche EU, Hoh CK, Hamilton MA, Fonarow GC, Hage A, et al. Exaggerated renal vasoconstriction during exercise in heart failure patients. Circulation 2000;101:784–89.
25. Middlekauff HR, Nitzsche EU, Hoh CK, Hamilton MA, Fonarow GC, Hage A, et al. Exaggerated muscle mechanoreflex control of reflex renal vasoconstriction in heart failure. J Appl Physiol 2001;90:1714–19.
26. Fulton RR, Meikle SR, Eberl S, Pfeiffer J, Constable CJ. Correction for head movements in positron emission tomography using an optical motion-tracking system. IEEE Trans Nucl Sci 2002;49:116–23.
27. Bloomfield PM, Spinks TJ, Reed J, Schnorr L, Westrip AM, Livieratos L, et al. The design and implementation of a motion correction scheme for neurological PET. Phys Med Biol 2003;48:959–78.
28. Woo SK, Watabe H, Choi Y, Kim KM, Park CC, Iida H. Sinogram-based motion correction of PET images using optical motion tracking system and list-mode data acquisition. IEEE Trans Nucl Sci 2004;51:782–88.
29. Herrero P, Staudenherz A, Walsh JF, Gropler RJ, Bergmann SR. Heterogeneity of myocardial perfusion provides the physiological basis of perfusable tissue index. J Nucl Med 1995;36:320–27.
30. Cselényi Z, Olsson H, Halldin C, Gulyás B, Farde L. A comparison of recent parametric neuroreceptor mapping approaches based on measurements with the high affinity PET radioligands [11C]FLB 457 and [11C]WAY 100635. Neuroimage 2006;32:1690–708.
31. Schuitemaker A, van Berckel BN, Kropholler MA, Kloet RW, Jonker C, Scheltens P, et al. Evaluation of methods for generating parametric (R-[11C]PK11195 binding images. J Cereb Blood Flow Metab 2007;27:1603–15.
32. Martin D, Sharma P, Salman K, Jones RA, Grattan-Smith JD, Mao H, et al. Individual kidney blood flow measured with contrast-enhanced first-pass perfusion MR imaging. Radiology 2008;246:241–48.
33. Iida H, Kanno I, Takahashi A, Miura S, Murakami M, Takahashi K, et al. Measurement of absolute myocardial blood flow with H2 15O and dynamic positron-emission tomography strategy for quantification in relation to the partial-volume effect. Circulation 1988;78:104–15.
34. Germano G, Chen BC, Huang S-C, Gambhir SS, Hoffman EJ, Phelps ME. Use of the abdominal aorta for arterial input function determination in the hepatic and renal PET studies. J Nucl Med 1992;33:613–20.

Use of a clinical MRI scanner for preclinical research on rats

Akihide Yamamoto · Hiroshi Sato · Jun-ichiro Enmi · Kenji Ishida ·
Takayuki Ose · Atsuomi Kimura · Hideaki Fujiwara · Hiroshi Watabe ·
Takuya Hayashi · Hidehiro Iida

Abstract This study evaluated the feasibility of imaging rat brains using a human whole-body 3-T magnetic resonance imaging (MRI) scanner with specially developed transmit-and-receive radiofrequency coils. The T_1- and T_2-weighted images obtained showed reasonable contrast. Acquired contrast-free time-of-flight magnetic resonance angiography images clearly showed the cortical middle cerebral artery (MCA) branches, and interhemispheric differences could be observed. Dynamic susceptibility contrast MRI at 1.17 mm³ voxel resolution, performed three times following administration of gadolinium diethylenetriamine pentaacetic acid (Gd-DTPA, 0.1 mmol/kg), demonstrated that the arterial input function (AIF) can be obtained from the MCA region, yielding cerebral blood flow (CBF), cerebral blood volume, and mean transit time (MTT) maps. The hypothalamus (HT) to parietal cortex (Pt) CBF ratio was 45.11 ± 2.85%, and the MTT was 1.29 ± 0.40 s in the Pt region and 2.32 ± 0.17 s in the HT region. A single dose of Gd-DTPA enabled the assessment of AIF within MCA territory and of quantitative CBF in rats.

Keywords Quantitative mapping · Human whole-body 3-T MRI scanner · Single dose of Gd-DTPA · Dynamic susceptibility contrast (DSC) · Preclinical research · Rat brain

1 Introduction

Magnetic resonance imaging (MRI) has been widely used in preclinical research on experimental small animals. Studies have typically been aimed at understanding the pathophysiologic status and evaluating the efficacy/side effects of newly developed treatments, such as pharmaceutical and regenerative medicine. Recently, a different idea has surfaced: the use of a human whole-body MRI scanner for small-animal imaging [1]. Although small-animal-dedicated scanners are superior to clinical scanners in terms of providing a better signal-to-noise ratio, the available pulse sequences are different from those in clinical scanners, and the magnetic field strength is often much higher. Small-animal imaging with clinical scanners is important for directly addressing clinical questions and/or identifying the origins of signal changes, including various disease conditions in a clinical setting.

Smith et al. [2] demonstrated that anatomic brain T_1- weighted (T_1W) images and T_2-weighted (T_2W) images can be obtained for healthy rats by using a 1-T clinical MRI scanner with a specially designed radiofrequency (RF) coil, given a reasonable spatial resolution (0.1953 × 0.1953 × 2.5 mm, 24 min of T_1W and 48 min of T_2W). The image contrast was sufficiently high to

A. Yamamoto · J. Enmi · K. Ishida · T. Ose · H. Watabe ·
T. Hayashi · H. Iida (✉)
Department of Investigative Radiology,
Advanced Medical Engineering Center,
National Cardiovascular Center Research Institute,
5-7-1, Fujishiro-dai, Suita, Osaka 565-8565, Japan
e-mail: iida@ri.ncvc.go.jp

A. Yamamoto · A. Kimura · H. Fujiwara · H. Watabe ·
T. Hayashi · H. Iida
Department of Medical Physics and Engineering,
Division of Health Sciences, Graduate School of Medicine,
Osaka University, 1-7, Yamada-oka, Suita,
Osaka 565-0871, Japan

H. Sato
Laboratory for Diagnostic Solution,
Advanced Medical Engineering Center,
National Cardiovascular Center Research Institute,
5-7-1, Fujishiro-dai, Suita, Osaka 565-8565, Japan

distinguish the cortical gray matter from the white matter [corpus callosum (CC)], as well as the lateral ventricle (LV) and interpeduncular cistern (IPC) from the thalamus (Thal). Guzman et al. [3] employed a clinical 1.5-T MRI scanner with a commercially available RF coil and demonstrated that both T_1W and T_2W images can be obtained with good contrast, a reasonable spatial resolution of $0.3125 \times 0.3125 \times 1.5$ mm, and an acquisition time of 19 min 51 s, as well as $0.35156 \times 0.375 \times 1.5$ mm at 8 min 34 s, corresponding to T_1W and T_2W images, respectively. Other investigators [4] applied a clinical 1.5-T MRI scanner with a 3-in.-diameter circular receive-only surface coil to assess anatomic images. Their images can be used to evaluate the pathophysiologic status of stroke [4] and cancer [5, 6], as well as the effects of neural excitotoxity [3]. There were also several studies that used a clinical 3-T MRI scanner fitted with commercial and/or hand-made RF coils to investigate the pathophysiology of stroke [7, 8] and brain tumors in rats [6, 9, 10]. Generally speaking, anatomic images with better contrast can be obtained in a stronger magnetic field, although there are additional factors that may influence the signal-to-noise ratio (SNR) or spatial resolution of anatomic images. Contrast-free time-of-flight magnetic-resonance angiography (TOF-MRA) can also be performed on rats; a reasonable spatial resolution was obtained by using a clinical 3-T MRI scanner with a single-turn solenoid coil [11].

Dynamic susceptibility contrast MRI (DSC-MRI) [12] has been widely used in clinical diagnosis, particularly in patients with stroke [13–19] and tumors [20]. The application of clinical MRI scanners has been extended to DSC-MRI studies of small animals with stroke [21, 22] and tumors [23] using a 1.5-T MRI scanner. Up to now, small-animal studies have been performed on 1.5-T MRI scanners only, and 3-T scanners have not been employed so far. This is largely attributed to the fact that the susceptibility-induced inhomogeneous magnetic field can cause more serious distortion of the images at a higher static magnetic field. In DSC-MRI studies, the echo planar imaging (EPI) technique is mainly used because fast acquisition is required for accurate tracking of the bolus passage of MR contrast agents. The EPI technique, however, is very sensitive to magnetic field inhomogeneity, and thus the EPI images of small-animal brains may be severely distorted. The gradient slew rate (SR) is not high enough to support a sufficiently short echo spacing period when clinical scanners are used for high spatial resolution imaging of small objects. Moreover, injected materials may cause further distortion [24]. The degree of distortion of dynamic EPI images of small-animal brains produced by a 3-T clinical scanner is currently unknown. The arterial input function (AIF) is also questionable. To the best of our knowledge, no DSC-MRI studies of small-animal brains on 3-T clinical scanners have been reported.

This study attempted to evaluate the feasibility of developing a human whole-body 3-T MRI system for small animals, particularly DSC-MRI with a single dose of gadolinium-diethylenetriamine pentaacetic acid (Gd-DTPA). The quality of various images—including the anatomic T_1W images, T_2W images, time-of-flight magnetic resonance angiography (TOF-MRA) images and DSC images—was tested, and the availability of the AIF obtained from rat brain was evaluated.

2 Materials and methods

2.1 Subjects

The subjects were three healthy adult rats supplied by Japan SLC, Inc. (Shizuoka, Japan). All three rats were males, and they ranged in age from 20 to 24 weeks. Their weight range was between 400 and 600 g. Anesthesia was administered with an intramuscular injection of ketamine (33 mg/kg; Daiichi-Sankyo Co., Ltd., Tokyo, Japan) and xylazine (6.6 mg/kg; Bayer Yakuhin, Ltd., Osaka, Japan). The first rat (Sprague Dawley, SD) was used for T_1-W and T_2W imaging of the whole brain. The second rat, also a SD, was used for contrast-free TOF-MRA imaging. The third was a Wistar rat, which was used for a Gd-DTPA (0.1 mmol/kg; Bayer Yakuhin, Ltd., Osaka, Japan)-enhanced DSC-MRI sequence. Experiments were carried out according to the protocol approved by the Local Committee for Laboratory Animal Welfare, National Cardiovascular Center, Osaka, Japan.

2.2 MRI acquisition

A human whole-body 3-T MRI scanner (Signa, GE Healthcare, Milwaukee, WI, USA) equipped with a 55-cm bore was employed in this study. The gradient coil system was capable of providing a maximum gradient amplitude of 40 mT/m and an SR of 150 T m^{-1} s^{-1}. All sequence programs employed in this study were designed for clinical studies.

Two solenoid coils designed for rats were specially developed to cover the whole brain, and were capable of both transmitting and receiving RF pulses. The three-turn solenoid coil, which had a diameter of 42 mm and a length along its cylindrical axis of 18 mm, was attached to an apparatus made from an acrylic mold, as shown in Fig. 1. All components of the stereotaxic apparatus consisted of nonmagnetic materials that fixed the head positions of the rats during data acquisition. The RF coil was designed to have an impedance of 50 Ω at a resonance frequency of
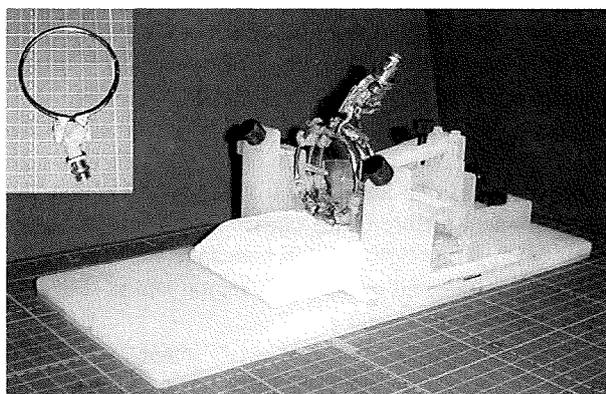
Fig. 1 The head fixation system for small animals, which was fitted with an MRI coil for RF transmission and reception. The coil is typically a three-turn solenoid; it can also be a single-turn coil, as shown on the *top left* of this figure

127.76 MHz. An additional single-turn surface coil of diameter 62 mm diameter was also developed for better homogeneity and was used for a single slice of DSC-MRI. The RF power in these coils had to be reduced to less than that used in the standard human head coil because of the diameter of the small coil. The transmission signal was therefore attenuated to 20 dB, which allowed the use of automated scanner software, including the calibration of the RF transmission power and receiver gains. All rats were fixed on the stereotaxic apparatus. They were placed at the center of the gantry and oriented with the craniocaudal axis perpendicular to the static magnetic field. Their heads were positioned inside the coil along the craniocaudal direction.

T_1W images were obtained with a conventional two-dimensional fast spin echo (2D-FSE) sequence. The repetition time (TR) was 1,500 ms [10]. The echo time (TE) was fixed at 14 ms. The echo train length (ETL) was 3. The field of view (FOV) was set at 40×30 mm^2, the slice thickness at 1.5 mm, the slice gap at 0.5 mm, the number of excitations (NEX) at 10, and the band width (BW) at 31.3 kHz. The acquired matrix (256×160) was interpolated, and null pixels were added in k-space to produce square matrices of 256×256. The acquisition time was 10 min 3 s.

T_2W images were obtained with a 2D-FSE and the following imaging parameters: TR, 4,100 ms; TE, 128 ms; ETL, 14; FOV, 40×30 mm; slice thickness, 1.5 mm; slice gap, 0.5 mm; NEX, 8; BW, 31.3 kHz; acquired matrix, 256×160, zero-filled to 256×256; phase direction, ventral-dorsal; acquisition time, 11 min 2 s.

Time-of-flight magnetic resonance angiography was performed using a three-dimensional flow-compensated spoiled gradient recalled (3D-SPGR) sequence prepared with magnetization transfer and with: TR, 53 ms; TE, 5.5 ms; flip angle (FA), 45°; BW, 16 kHz; FOV, 8×6 cm;

slice thickness, 0.2 mm; one acquired slab of $512 \times 512 \times 64$; voxel resolution, $0.156 \times 0.156 \times 0.2$ mm^3; NEX, 1; acquisition time, 21 min 46 s.

Dynamic susceptibility contrast images were obtained following the intravenous administration of Gd-DTPA to the T_2^*-weighted gradient echo dynamic images. A bolus of Gd-DTPA (0.1 mmol/kg) was injected manually into the tail vein with a 22-gauge catheter via 1 m of polyethylene tubing (PE50, internal diameter: 0.58 mm/outer diameter: 0.965 mm, Becton Dickinson and Company, Franklin Lakes, NJ, USA), and was followed by an additional administration of saline (1.0 ml). A multishot EPI (number of shots = 2) was employed to improve EPI distortion and temporal resolution. The imaging parameters were: TR, 142 ms; TE, 22.1 ms; FA, 20°; FOV, 40×40 mm; matrix size, 64×64, leading to a pixel size of 0.625×0.625 mm^2. The slice thickness was 3 mm in a single slice around the hypothalamus (HT). The temporal resolution was 0.284 s per image, and the acquisition time was 1 min 15 s. This assessment was repeated three times at intervals of 40 min and 10 min, corresponding to the first–second and second–third scans, respectively.

2.3 Data analysis

All MRI images were reconstructed on the same workstation provided for the GE Signa 3-T scanner used for the clinical programs. The images were then transferred to a Linux workstation. Lastly, data analysis was carried out using in-house and commercial software.

To evaluate the T_1W and T_2W image quality, we calculated the contrast-to-noise ratio (CNR) with an inter-tissue method [25–27] as follows: CNR $= (\pi/2)^{1/2} (SI_a - SI_b)/SI_{air}$, where SI_{air} represents the mean signal intensity of air, and SI_a and SI_b represent the signal intensities of tissue a and tissue b, respectively.

Angiograms were created by generating the partial maximum intensity projection (MIP) with commercial software [Virtual Place Liberty (VPL), AZE Co. Ltd., Tokyo, Japan]. Visible middle cerebral artery (MCA) branches and left-to-right differences in MCA were carefully investigated.

For the DSC images of slice sections containing the internal carotid artery (ICA) and/or MCA, a series of images were carefully observed. A region of interest (ROI) was carefully selected in the MCA region, from which the AIF was obtained, with the help of other anatomic information. To avoid susceptibility artifacts caused by air in the trachea, the area of the arterial circle of Willis was excluded from the definition of the AIF. The anterior cerebral artery was also excluded because of possible susceptibility effects attributed to venous blood. A Gaussian filter of full width at half maximum (FWHM) 1.1 mm

was applied to all dynamic images. The time versus signal intensity curves (TICs) were converted to the Gd-DTPA concentration according to Eq. 1 given in the "Appendix." Functional mapping images of the mean transit time (MTT), cerebral blood volume (CBV), and cerebral blood flow (CBF) were carried out with the deconvolution method [28]. The theory behind this is described in detail in the "Appendix." For ROI analysis, images of matrix size 64 × 64 were converted to 256 × 256 using a sinc interpolation function.

3 Results

T_1W and T_2W images reconstructed with a spatial resolution of 0.156 × 0.188 × 1.5 mm are shown in Fig. 2. White matter could be discriminated from cortical and deep gray matter regions. The locations of small anatomic features such as the caudate putamen (CPu), striatum, the CC, and the hippocampus (HC) could also be identified in both T_1W and T_2W anatomic images. The CNRs between the HC and CC were 15.6 and 9.8, respectively, for the T_1W and T_2W images shown in Fig. 2. The CNRs between the HC and IC were 23.2 and 13.6, respectively, although the CNR may be underestimated due to the contamination of signal from the globus pallidus.

Results for MIP images obtained with contrast-free TOF-MRA are shown in Fig. 3. Coronal MIP images around the HT of thickness 5 mm are shown in Fig. 3a. In this figure, the slice section contained ICAs and MCA. The MCA, the cortical branches in both the left and right hemispheres, can be identified. It is important to note that the anatomic structure of the cortical MCA arteries is different between the right and left hemispheres. The ROI for the AIF was selected in the MCA region and is shown by the arrows in Fig. 3a and b.

A typical example of a DSC-MRI image is shown in Fig. 4. Distortion of the DSC-MRI images is visible in Fig. 4A in the phase direction. A magnified area from dynamic images of the MCA region (shown as a rectangle in Fig. 4A) is displayed in Fig. 4B. Several pixels indicate temporal changes in pixel contrast as a function of time, and these are reflected by Gd-DTPA negative enhancement. The pixel signal intensity varied as shown in Fig. 4C, and the curve shown was employed to estimate the AIF. Figure 5 shows the TIC in this area together with the TIC for the whole brain region obtained from each of the three scans. The curves were visually reproducible in terms of the shapes, heights and widths of the curves around the peak, as well as the tail height at the end of the scan. It should also be noted that the baseline was consistent before each injection of Gd-DTPA, even though the second and

Fig. 2 T_1W images (top) and T_2W images (bottom) obtained from an SD rat, with the following anatomic locations as indicated: the somatosensory cortex (SS), corpus callosum (CC), parietal cortex (Pt), external capsule (EC), caudate putamen (CPu), internal capsule (IC), hippocampus (HC), thalamus (Thal), auditory cortex (Au), amygdala (AM), hypothalamus (HT), internal carotid arterial system (ICAs), trigeminal nerve (TN), interpeduncular cistern (IPC), dorsal third ventricle (D3V), and the lateral ventricle (LV). These slice sections were located −1.5 mm (left) and −3.5 mm (right), respectively, from the bregma
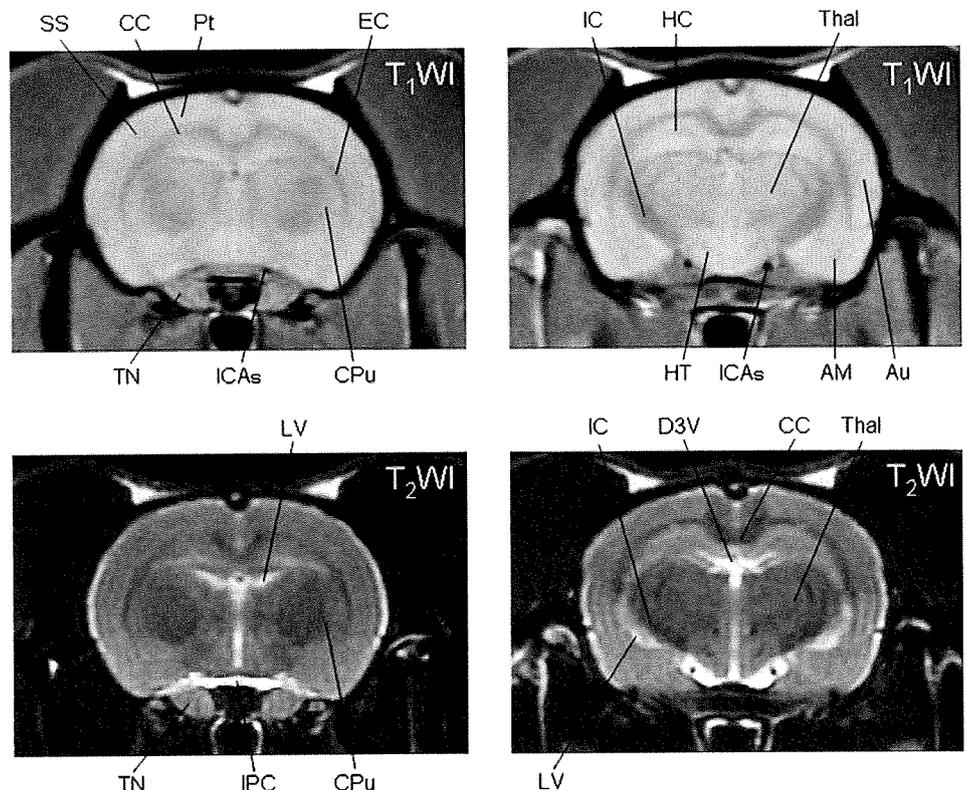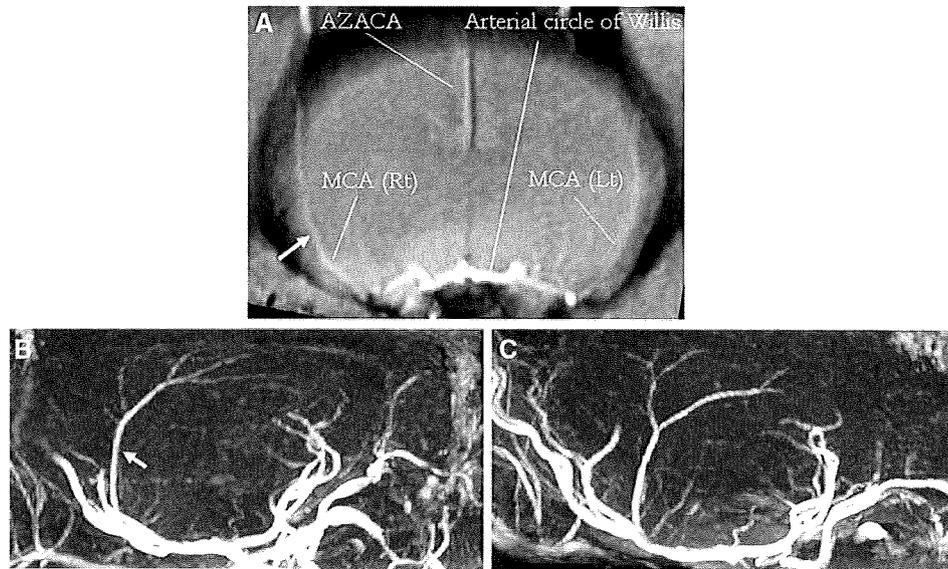
Fig. 3 Partial maximum intensity projection maps of contrast-free time-of-flight MRA obtained for a Sprague Dawley rat. Maps represent areas around the Thal (**a**), right hemisphere (**b**), and left hemisphere (**c**). The *white arrows* indicate the selected ROI level (as described in the "Discussion"). *AZACA*, azygos anterior cerebral artery

Fig. 4 Typical time-frame images obtained from Gd-bolus tracking T_2*-weighted dynamic images (after the first injection). A *white rectangle* was placed in the MCA area (**a**), and magnified images of this rectangle were visualized as *a*, *b*, *c*, *d*, and *e* in **b**. The TIC within the pixels is indicated by *white arrows* in **b**. The data were then plotted in a graph (**c**). Typical data points were extracted from the first injection at the times of 9.2 (*a*), 16.4 (*b*), 18.1 (*c*), 20.1 (*d*), and 33.9 (*e*) s. The phase direction is shown as a *white arrow* in **a**
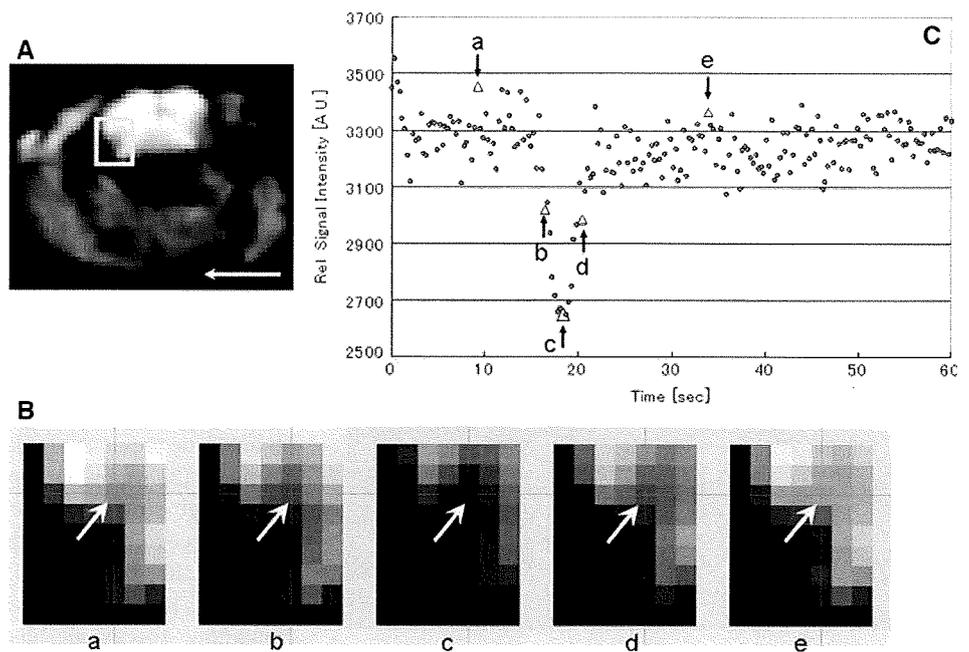
the third curves should have been affected by the previous injection of Gd-DTPA.

Functional mapping images of CBF, CBV, and MTT calculated according to the theory described in the "Appendix" are shown in Fig. 6. Images obtained from this sequential assessment appeared to be reasonably clear, although slightly noisy, and were consistent among the scans. The absolute CBFs (mean ± SD) in the cortical gray matter area (mainly the parietal cortex, Pt) were 24.04 ± 2.88, 17.75 ± 3.34, and 31.87 ± 7.27 ml g^{-1} min^{-1} for the first, second, and third scans, respectively. The HT-to-Pt CBF ratios were 46.7, 51.5, and 43.0% for the first, second, and third scans, respectively. The CBVs were 0.49 (0.44), 0.50 (0.35), and 0.47 (0.41) ml/ml in the Pt (the HT) region in the first, second, and third scans, respectively. The MTTs in the same regions were 1.22 (2.51), 1.72 (2.29),

Fig. 5 TIC dynamic changes in the whole brain are shown in the first injection (a), the second injection (b), and the third injection (c). For each injection, a one-pixel ROI was selected and observed, as shown for the first (d), second (e) and third (f) injections, respectively. The negative enhancement changes in the rate from peak signal intensity to baseline were 16.8% (a), 10.0% (b), and 10.3% (c) at the whole brain (average 12.3, SD 3.9). The peak-to-base fractions at selected ROIs were 19.2% (d), 14.5% (e), and 16.9% (f) (average 16.9, SD 2.3), for the first, second, and third injections, respectively
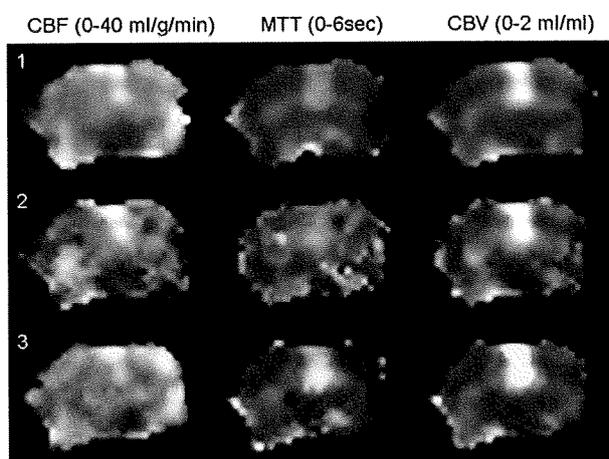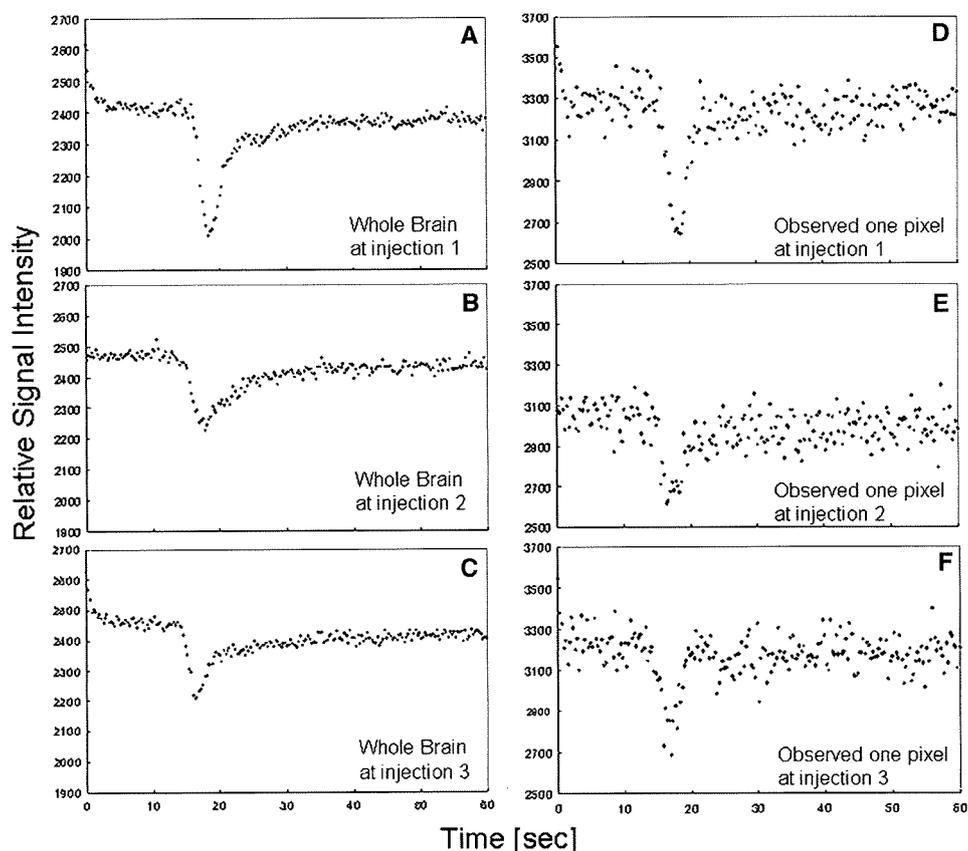

Fig. 6 *First column on the left*: CBF maps using the AIF from MCA, pictured in a grayscale from 0 to 4 ml g^{-1} min^{-1}. MTT maps are shown in the *middle column*, followed by CBV maps of 0–2 ml g^{-1} min^{-1} in the *column on the right*. Deconvolution was carried out pixel by pixel with b-SVD and then smoothed to 0.15625 × 0.15625 mm in-plane resolution from the acquired voxel resolution of 0.625 × 0.625 × 3 mm (1.17 mm^3) in DSC-MRI

and 0.92 (2.16) s in each of the three scans. Among the three injections, the absolute MTTs (mean ± SD) were 1.29 ± 0.40 s in the Pt and 2.32 ± 0.17 s in the HT region.

4 Discussion

This study demonstrated that our system of a human whole-body 3-T MRI fitted with an in-house solenoid coil developed for small animals can provide morphologic and functional images of the rat brain in vivo. The quality of T_1W and T_2W images obtained with a scan duration of approximately 10 min was better than those obtained in previous studies in which 1.5-T clinical MRI scanners [3] were employed. The neocortex and large subcortical structures, such as the Thal and HC, are readily recognized from their topographic relationship to the CC, the ventricular system, and the subarachnoid space [2]. In T_1W images, the cerebrospinal fluid (CSF)-containing spaces are visible as they are hypointense, and the arterial flow showed a signal loss caused by so-called flow void effects, which is typically seen in the spin echo sequence [2]. In T_2W images, the CSF was bright and white (prolonged T_2 relaxation time), whereas the myelinated white matter was black (short T_2 relaxation time). The white matter tracts such as the IC and CC were clearly visible in both T_1W and T_2W images, and better quality was obtained compared to previous reports employing 1.0- and 1.5-T clinical MRI scanners [2, 3].

Magnetic resonance angiography images also clearly showed the structure of the distal MCA branches. The MRA findings of interhemispheric differences with regards to MCA in the SD rat were also consistent with a previous report on Wistar rats [29], which indicated left-to-right asymmetric structure in three out of ten Wistar rats using a 7-T MRI scanner dedicated to small-animal imaging [29]. Our MRA images are superior to those obtained in previous work [11] that employed a clinical 3-T MRI scanner and that only showed the major cerebral arteries and the carotid arteries because they focused mainly on validating occlusion models [11]. The superior quality of our MRA images can largely be attributed to the type of RF coil we used. Ours is a three-turn solenoid coil that covers only the cerebral area, whereas the previous work [11] employed a single-turn coil (diameter of 6.4 cm and length of 10 cm) that covered the whole head, including the brain and the neck. Additionally, the prolonged acquisition period in our study (almost 20 min) compared to the acquisition period used in the previous study [11] (almost 4 min) may have been a factor that led to higher-quality MRA images.

An important point about this study is that DSC-MRI images of reasonable quality can also be obtained with a clinical MRI scanner at 3 T on rats. In addition, we were able to extract the AIF from the rat brain, which is an important accomplishment. Selection of an ROI in the MCA region successfully provided the AIF. Spatial distortion or susceptibility artifacts were not visible in our observations. Signal changes were obtained during DSC-MRI following a single dose of Gd-DTPA. During this study, the dedicated transmit and receive RF coils were considered to be crucial to obtaining a reasonable SNR. Our study was performed with the same sequence and the same dose rate (0.1 mmol/kg) of Gd-DTPA that are commonly used in clinical examinations. Moreover, it was performed with high (1.17 mm^3)-resolution dynamic imaging.

The quantitative images of CBF were consistent with those in a previous report on the use of [^{14}C] iodoantipyrine [30]. Namely, the HT-to-Pt contrast in CBF was 43–52% in this study, which is close to the values reported by Bloom et al. [30] of 44–58%. Although the absolute CBF and CBV values in our study were different from those obtained previously [13, 30, 31], the uncertain scaling factors for each of these were canceled out when calculating the MTT with Eq. 5 [32] (see also the "Appendix"). The MTT obtained in this study was comparable to those obtained in previous work [31, 33].

We noticed that the absolute CBF and CBV values were overestimated, which suggests that some limitations apply, such as the partial volume effect (PVE) caused by insufficient spatial resolution as compared with the anatomic structure of the MCA. Detection of AIF with a repeat injection was performed (Fig. 5, right row). The major MCA diameter was approximately 0.5 mm at the maximum, as evaluated from Fig. 3, which suggested that the measured AIF is largely influenced by the PVE [24]. Also, the differences in absolute value may be due to the fact that a nonlinear relationship exists between the signal intensity and the contrast agent concentration. Previous reports have proposed nonlinearity correction methods for brain tissue [34] and AIF [35]. Further studies are needed to confirm the accuracy and the reproducibility [36]. Image distortion caused by dielectric effects [37] and/or EPI distortion [38] are other sources of error, and should be investigated systematically.

Improving the quality of the original dynamic images acquired would also improve the mapping image quality. In order to achieve better detection of the dynamic susceptibility contrast caused by T_2^* signals, the optimization of TE, FA and the acquisition matrix should be investigated. We speculate that a multichannel phased array coil and parallel imaging techniques would reduce the level of distortion. The DSC-MRI in this study was obtained for only a single slice. Further careful attention is needed to perform multislice imaging in order to minimize inflow effects [35]. In our study, the contrast concentration $C(t)$ curves including the AIFs varied slightly among the three injections. A sophisticated injector system that is MR-compatible may improve the variation.

A dedicated high magnetic field scanner equipped with a dedicated small bore is the optimal device for small-animal imaging. However, such systems are not commonly available. The system developed in this study might serve as a low-cost solution or an alternative. The use of the present system provides an opportunity to use the same imaging platform available for clinical studies for small-animal imaging [7]. This would allow us to determine pathophysiological status from MRI signals using animal models with various diseases. More importantly, the optimization of several scan parameters, which has been difficult to achieve in clinical patients, can easily be performed on small animals with this system. In particular, the reproducibility of the assessment of CBF with DSC-MRI, which has been reported to be a limitation on clinical studies [19, 36], could be improved by performing a systematic evaluation of each scan parameter when this system is used on small animals rather than clinical patients. With the addition of a high-strength insert gradient coil [39], which allows for thinner slices and much faster read-out, the system performance and the spatial resolution with an acceptable SNR can be improved. The use of adapting coils could be an effective solution for those who operate MR scanners for human subjects and intend to gain experience [40] in preclinical research.

5 Conclusion

In this preclinical study on rats, reasonable image quality was obtained for T_1W, T_2W, and contrast-free TOF-MRA images generated using a human whole-body 3-T MRI scanner and a newly developed solenoid coil. In DSC-MRI, this system visualized transient signal changes with a single dose of Gd-DTPA and using the same sequences commonly used in clinical examinations. A human whole-body 3-T MRI scanner and dedicated coil make it possible to detect the AIF in the MCA region of Wistar rats. High-resolution DSC-MRI was accomplished with a clinical scanner, but the spatial resolution with an acceptable SNR was insufficient for the rat brain. Although there may be some remaining issues relating to AIF, we have shown the potential of DSC-MRI in our study.

Appendix: Calculation of functional mapping images from DSC-MRI

The observed TIC $S(t)$ was converted to a time-versus-concentration curve (TCC) $C(t)$ by the following equation [16, 36]:

$$C(t) = k \cdot \Delta R2^*(t) = -k \cdot \ln(S(0)/S(t))/\text{TE}, \tag{1}$$

where $\Delta R2^*$ is the change in the T_2^* relaxation rate and k is a constant. In this study, it was assumed that $k = 1$. $S(0)$ is the pre-contrast (baseline) signal and $S(t)$ is the measured signal at time t. The next step was to fit this first-pass period of TCC to a gamma variate function:

$$C(t) = a(t - b)^c \exp(-(t - b)/d), \tag{2}$$

where a, b, c, and d were determined by nonlinear least-squares fitting. To minimize the effects of the recirculation of the contrast agent, data were neglected in the fit if these concentrations were less than 50% of the maximum after the peak of the TCC.

The fitted tissue TCC $Ct(t)$ was deconvolved by the fitted AIF $C_{\text{AIF}}(t)$ by using singular value decomposition with a block-circulant deconvolution matrix (b-SVD) method [28] according to the equation

$$\text{CBF} \cdot R(t) = Ct(t) \otimes^{-1} C_{\text{AIF}}(t), \tag{3}$$

where $\otimes^{-1}$ represents the deconvolution operator and $R(t)$ is a residue function representing the tissue response to an instantaneous bolus. $\text{CBF} \cdot R(t)$ was estimated by deconvolving $Ct(t)$ by $C_{\text{AIF}}(t)$ using b-SVD, and then CBF was determined as the maximum value of the obtained $\text{CBF} \cdot R(t)$.

The CBV was calculated as follows:

$$\text{CBV} = \int_0^\infty Ct(t)\mathrm{d}t \bigg/ \int_0^\infty C_{\text{AIF}}(t)\mathrm{d}t. \tag{4}$$

Lastly, the MTT is calculated from CBF and CBV by applying the central volume principle [32]:

$$\text{MTT} = \text{CBV}/\text{CBF}. \tag{5}$$

References

1. Brockmann MA, Kemmling A, Groden C. Current issues and perspectives in small rodent magnetic resonance imaging using clinical MRI scanners. Methods. 2007;43:79–87.
2. Smith DA, Clarke LP, Fiedler JA, Murtagh FR, Bonaroti EA, Sengstock GJ, et al. Use of a clinical MR scanner for imaging the rat brain. Brain Res Bull. 1993;31(1–2):115–20.
3. Guzman R, Lövblad KO, Meyer M, Spenger C, Schroth G, Widmer HR. Imaging the rat brain on a 1.5 T clinical MR-scanner. J Neurosci Methods. 2000;97(1):77–85.
4. Fujioka M, Taoka T, Matsuo Y, Hiramatsu KI, Sakaki T. Novel brain ischemic change on MRI: delayed ischemic hyperintensity on T_1-weighted images and selective neuronal death in the caudoputamen of rats after brief focal ischemia. Stroke. 1999;30(5):1043–6.
5. Thorsen F, Ersland L, Nordli H, Enger PO, Huszthy PC, Lundervold A, et al. Imaging of experimental rat gliomas using a clinical MR scanner. J Neurooncol. 2003;63(3):225–31.
6. Biswas J, Nelson CB, Runge VM, Wintersperger BJ, Baumann SS, Jackson CB, et al. Brain tumor enhancement in magnetic resonance iimaging: comparison of signal-to-noise ratio (SNR) and contrast-to-noise ratio (CNR) at 1.5 versus 3 Tesla. Invest Radiol. 2005;40:792–7.
7. Shimamura M, Sato N, Sata M, Kurinami H, Takeuchi D, Wakayama K, et al. Delayed postischemic treatment with fluvastatin improved cognitive impairment after stroke in rats. Stroke. 2007;38:3251–8.
8. Lee JM, Zhai G, Liu Q, Gonzales ER, Yin K, Yan P, et al. Vascular permeability precedes spontaneous intracerebral hemorrhage in stroke-prone spontaneously hypertensive rats. Stroke. 2007;38:3289–91.
9. Wintersperger BJ, Runge VM, Biswas J, Reiser MF, Schoenberg SO. Brain tumor enhancement in mr imaging at 3 Tesla: comparison of SNR and CNR gain using TSE and GRE techniques. Invest Radiol. 2007;42:558–63.
10. Sato H, Enmi J, Teramoto N, Hayashi T, Yamamoto A, Tsuji T, et al. Comparison of Gd-DTPA-induced signal enhancements in rat brain C6 glioma among different pulse sequences in 3-Tesla magnetic resonance imaging. Acta Radiol. 2008;49:172–9.
11. Yang YM, Feng X, Yao ZW, Tang WJ, Liu HQ, Zhang L. Magnetic resonance angiography of carotid and cerebral arterial

occlusion in rats using a clinical scanner. J Neurosci Methods. 2008;167(2):176–83.

12. Rosen BR, Belliveau JW, Vevea JM, Brady TJ. Perfusion imaging with NMR contrast agents. Magn Reson Med. 1990;14(2):249–65.

13. Calamante F, Thomas DL, Pell GS, Wiersma J, Turner R. Measuring cerebral blood flow using magnetic resonance imaging techniques. J Cereb Blood Flow Metab. 1999;19(7):701–35.

14. Yamada K, Wu O, Gonzalez RG, Bakker D, Østergaard L, Copen WA, et al. Magnetic resonance perfusion-weighted imaging of acute cerebral infarction: effect of the calculation methods and underlying vasculopathy. Stroke. 2002;33(1):87–94.

15. Tamura H, Hatazawa J, Toyoshima H, Shimosegawa E, Okudera T. Detection of deoxygenation-related signal change in acute Ischemic stroke patients by T2*-weighted magnetic resonance imaging. Stroke. 2002;33(4):967–71.

16. Calamante F, Gadian DG, Connelly A. Quantification of perfusion using bolus tracking magnetic resonance imaging in stroke: assumptions, limitations, and potential implications for clinical use. Stroke. 2002;33(4):1146–51.

17. Latchaw RE, Yonas H, Hunter GJ, Yuh WT, Ueda T, Sorensen AG, et al. Guidelines and recommendations for perfusion imaging in cerebral ischemia: a scientific statement for healthcare professionals by the Writing Group on Perfusion Imaging, from the Council on Cardiovascular Radiology of the American Heart Association. Stroke. 2003;34(4):1084–104.

18. Carroll TJ, Rowley HA, Haughton VM. Automatic calculation of the arterial input function for cerebral perfusion imaging with MR imaging. Radiology. 2003;227(2):593–600.

19. Wintermark M, Sesay M, Barbier E, Borbély K, Dillon WP, Eastwood JD, et al. Comparative overview of brain perfusion imaging techniques. Stroke. 2005;36(9):83–99.

20. Bruening R, Kwong KK, Vevea MJ, Hochberg FH, Cher L, Harsh GR 4th, et al. Echo-planar MR determination of relative cerebral blood volume in human brain tumors: T1 versus T2 weighting. AJNR Am J Neuroradiol. 1996;17(5):831–40.

21. Chen F, Suzuki Y, Nagai N, Peeters R, Coenegrachts K, Coudyzer W, et al. Visualization of stroke with clinical MR imagers in rats: a feasibility study. Radiology. 2004;233:905–11.

22. Chen F, Suzuki Y, Nagai N, Sun X, Coudyzer W, Yu J, et al. Delayed perfusion phenomenon in a rat stroke model at 1.5 T MR: An imaging sign parallel to spontaneous reperfusion and ischemic penumbra? Eur J Radiol. 2007;61:70–8.

23. Fan G, Zang P, Jing F, Wu Z, Guo Q. Usefulness of diffusion/perfusion-weighted MRI in rat gliomas: correlation with histopathology. Acad Radiol. 2005;12(5):640–51.

24. van Osch MJ, van der Grond J, Bakker CJ. Partial volume effects on arterial input functions: shape and amplitude distortions and their correction. J Magn Reson Imaging. 2005;22(6):704–9.

25. Wada Y, Hara T, Miyati T. Basic assessment of the CNR measurement method of MRI system in phantom—suggestion for improvement in the CNR evaluation method. Nippon Hoshasen Gijutsu Gakkai Zasshi. 2008;64(2):268–76.

26. Ogura A, Maeda F, Miyai A, Hongoh T. Accuracy of contrast-to-noise ratio measurement for magnetic resonance clinical images. Nippon Hoshasen Gijutsu Gakkai Zasshi. 2004;60(11):1543–9.

27. Miyati T. Image quality assessment in magnetic resonance imaging. Nippon Hoshasen Gijutsu Gakkai Zasshi. 2002;58(1):40–8.

28. Wu O, Ostergaard L, Weisskoff RM, Benner T, Rosen BR, Sorensen AG. Tracer arrival timing-insensitive technique for estimating flow in MR perfusion-weighted imaging using singular value decomposition with a block-circulant deconvolution matrix. Magn Reson Med. 2003;50:164–74.

29. Besselmann M, Liu M, Diedenhofen M, Franke C, Hoehn M. MR angiographic investigation of transient focal cerebral ischemia in rat. NMR Biomed. 2001;14(5):289–96.

30. Bloom AS, Tershner S, Fuller SA, Stein EA. Cannabinoid-induced alterations in regional cerebral blood flow in the rat. Pharmacol Biochem Behav. 1997;57(4):625–31.

31. Shockley RP, LaManna JC. Determination of rat cerebral cortical blood volume changes by capillary mean transit time analysis during hypoxia, hypercapnia and hyperventilation. Brain Res. 1998;454(1–2):170–8.

32. Meier P, Zierler KL. On the theory of the indicator-dilution method for measurement of blood flow and volume. J Appl Physiol. 1954;6:731–44.

33. Johansson E, Månsson S, Wirestam R, Svensson J, Petersson JS, Golman K, et al. Cerebral perfusion assessment by bolus tracking using hyperpolarized 13C. Magn Reson Med. 2004;51(3):464–72.

34. Enmi J, Hayashi T, Watabe H, Moriwaki H, Yamada N, Iida H. Measurement of cerebral blood flow with dynamic susceptibility contrast MRI and comparison with O-15 positron emission tomography. Int Congr Ser. 2004;1265:150–8.

35. Calamante F, Vonken EJ, van Osch MJ. Contrast agent concentration measurements affecting quantification of bolus-tracking perfusion MRI. Magn Reson Med. 2007;58:544–53.

36. Grandin CB, Bol A, Smith AM, Michel C, Cosnard G. Absolute CBF and CBV measurements by MRI bolus tracking before and after acetazolamide challenge: repeatability and comparison with PET in humans. Neuroimage. 2005;26:525–35.

37. Kuhl CK, Träber F, Schild HH. Whole-body high-field-strength (3.0-T) MR imaging in clinical practice. Part I. Technical considerations and clinical applications. Radiology. 2008;246(3):675–96.

38. Jezzard P, Clare S. Sources of distortion in functional MRI data. Hum Brain Mapp. 1999;8(2–3):80–5.

39. Mayer D, Zahr NM, Adalsteinsson E, Rutt B, Sullivan EV, Pfefferbaum A. In vivo fiber tracking in the rat brain on a clinical 3T MRI system using a high strength insert gradient coil. Neuroimage. 2007;35(3):1077–85.

40. Graf H, Martirosian P, Schick F, Grieser M, Bellemann ME. Inductively coupled rf coils for examinations of small animals and objects in standard whole-body MR scanners. Med Phys. 2003;30(6):1241–5.

A physiologic model for recirculation water correction in CMRO$_2$ assessment with $^{15}O_2$ inhalation PET

Nobuyuki Kudomi, Takuya Hayashi, Hiroshi Watabe, Noboru Teramoto, Rishu Piao, Takayuki Ose, Kazuhiro Koshino, Youichirou Ohta and Hidehiro Iida

Department of Investigative Radiology, Advanced Medical-Engineering Center, National Cardiovascular Center Research Institute, Osaka, Japan

Cerebral metabolic rate of oxygen (CMRO$_2$) can be assessed quantitatively using $^{15}O_2$ and positron emission tomography. Determining the arterial input function is considered critical with regards to the separation of the metabolic product of $^{15}O_2$ (RW) from a measured whole blood. A mathematical formula based on physiologic model has been proposed to predict RW. This study was intended to verify the adequacy of that model and a simplified procedure applying that model for wide range of species and physiologic conditions. The formula consists of four parameters, including of a production rate of RW (k) corresponding to the total body oxidative metabolism (BMRO$_2$). Experiments were performed on 6 monkeys, 3 pigs, 12 rats, and 231 clinical patients, among which the monkeys were studied at varied physiologic conditions. The formula reproduced the observed RW. Greater k values were observed in smaller animals, whereas other parameters did not differ amongst species. The simulation showed CMRO$_2$ sensitive only to k, but not to others, suggesting that validity of determination of only k from a single blood sample. Also, k was correlated with BMRO$_2$, suggesting that k can be determined from BMRO$_2$. The present model and simplified procedure can be used to assess CMRO$_2$ for a wide range of conditions and species.
Journal of Cerebral Blood Flow & Metabolism advance online publication, 5 November 2008; doi:10.1038/jcbfm.2008.132

Keywords: arterial input; CMRO$_2$; mathematical modeling; recirculation water; PET

Introduction

Cerebral metabolic rate of oxygen (CMRO$_2$) can be quantitatively assessed using ^{15}O-labeled oxygen ($^{15}O_2$) and positron emission tomography (PET). This technique is based on an estimation of influx rate of $^{15}O_2$ to the cerebral tissue from arterial blood. Using information of cerebral blood flow (CBF) that may be obtained either from a separate scan with ^{15}O-labeled water (H$_2^{15}$O) or from the clearance rate $^{15}O_2$ of tissue,

the oxygen extraction fraction (OEF) can also be calculated. The arterial input function must be determined before beginning this calculation. More specifically, a metabolic product of $^{15}O_2$ in the arterial blood, as a form of ^{15}O-labeled water (i.e., recirculating ^{15}O-water or RW) needs to be accurately estimated.

The arterial whole blood radioactivity curve can be obtained by measuring the radioactivity concentration of continuously withdrawn whole blood using a monitoring device (Eriksson et al, 1988; Eriksson and Kanno, 1991; Votaw and Shulman, 1998; Kudomi et al, 2003). Assessment of a time-dependent RW curve may be achieved by separating the plasma from the whole blood samples. This, however, requires labor-intensive procedures of frequent, manual arterial blood samplings, the centrifugation of all collected blood samples, and radioactivity measurements for both whole blood and plasma (Holden et al, 1988).

Ohta et al (1992) proposed to neglect the component of RW from the arterial input function. This technique fits three parameters of CMRO$_2$, CBF, and

2

cerebral blood volume (CBV) to the kinetic $^{15}O_2$ data obtained from a single PET scan after the bolus administration of $^{15}O_2$. To minimize errors which result from neglecting RW, only the initial 3 mins of data after the bolus inhalation of $^{15}O_2$ were used when calculating the parameters. This approach has been applied to evaluate the magnitude of increase in $CMRO_2$ relative to that in CBF during cognitive stimulation tasks (Fujita et al, 1999; Vafaee and Gjedde, 2000; Okazawa et al, 2001a,b; Yamauchi et al, 2003; Mintun et al, 2002), but one of the drawbacks to this technique is the lack of accurate statistics, which is due to the use of a short scan duration.

Iida et al (1993) have developed a mathematical formula to predict the production of RW based on a physiologic model, which allows prolongation of the PET acquisition period with an additional statistical accuracy. The formula assumes a fixed rate constant for production of RW from $^{15}O_2$ in the body. This is based on the fact that the observed rate constant did not vary among clinical subjects, and thus causes nonsignificant errors in $CMRO_2$. However, the study is limited only to human subjects studied at rest, and results have not been verified using other species such as rat and mouse (Magata et al, 2003; Temma et al, 2006; Yee et al, 2006). Also, the findings have not been evaluated on humans who are under physiologic stress, though under such conditions the whole-body oxygen consumption is expected to change. Moreover, it is important to extend the approach to physiologically stressed conditions as recent progress for assessing $CMRO_2$ and CBF simultaneously from a short period dynamic scan by using a dual tracer autoradiography (DARG) (Kudomi et al, 2005). The DARG has enabled the $^{15}O_2$ PET to assess $CMRO_2$ and CBF simultaneously at various physiologically activated conditions.

The aim of this study is to verify the method used to estimate the arterial RW during the $^{15}O_2$ inhalation for simultaneous determination of $CMRO_2$ and CBF from the rapid procedures of $^{15}O_2$ PET. The feasibility of a simplified procedure is also being investigated. Applicability of this approach was tested for a wide range of species under various physiologic conditions. Experiments were designed to apply for different species as well as different physiologic conditions. A simulation study was also performed to evaluate the level of error sensitivity associated with this approach.

Materials and methods

Theory

Variables used in the recirculating water model are summarized in Table 1. The mathematical model that formulates the time-dependent RW in arterial blood consists of three rate constants: (1) the production rate of RW or k (per min), proportional to oxidative metabolism in the total body system ($BMRO_2$), (2) the forward diffusion rate (k_w, per min) of the metabolized ^{15}O-water between the blood and interstitial spaces in the body, and (3) the backward diffusion rate (k_2, per min) of the metabolized ^{15}O-water between the blood and interstitial spaces in the body. The differential equations for the arterial activity concentration of ^{15}O-water at a time t (secs) ($A_w(t)$, Bq/mL), after the physical decay correction can be expressed as follows (Huang et al, 1991):

$$\frac{d}{dt}A_w(t) = k \cdot A_o(t) - k_w \cdot A_w(t) + k_2 \cdot C(t) \quad (1a)$$

$$\frac{d}{dt}C(t) = k_w \cdot A_w(t) - k_2 \cdot C(t) \quad (1b)$$

$$A_t(t) = A_o(t) + A_w(t) \quad (1c)$$

where $A_o(t)$ and $A_t(t)$ denote the radioactivity concentration of the arterial $^{15}O_2$ and the total radioactivity from both

Table 1 Variables used in the recirculating water model

Symbol	Description	Unit
A_o	Radioactivity concentration of arterial $^{15}O_2$	Bq/mL
A_w	Radioactivity concentration of arterial $H_2^{15}O$	Bq/mL
A_t	Total radioactivity concentration from arterial $^{15}O_2$ and $H_2^{15}O$	Bq/mL
A_{plasma}	Radioactivity concentration of arterial plasma	Bq/mL
C	Activity concentration of $H_2^{15}O$ in peripheral tissue in a body	Bq/mL
Fi_{O_2}	Oxygen concentration in inhaled gas	%
Fe_{O_2}	Oxygen concentration in expired gas	%
k	Production rate of recirculating $H_2^{15}O$	per min
k_{BM}	Production rate of recirculating $H_2^{15}O$ obtained from BM approach	per min
k_w	Forward diffusion rate of $H_2^{15}O$ from blood to body interstitial space	per min
k_2	Backward diffusion rate of $H_2^{15}O$ from blood to body interstitial space	per min
λ	Decay constant of ^{15}O ($=0.00567$ per sec)	per sec
v	Stroke volume	mL
p	k_w/k_2	
r	Respiration rate	per min
R	Fractional water content ratio in whole blood to that in the plasma	
R_{O_2}	Rate of oxidative metabolism in the whole-body system	mL/min
Δt	Delayed appearance time of recirculating water	secs
V_{O_2}	Total volume of molecular oxygen in total blood	mL
V_{TB}	Total volume of blood in a body	mL

$^{15}O_2$ and $H_2^{15}O$, respectively. $C(t)$ is an activity concentration of $H_2^{15}O$ in the peripheral tissue of the total body. Assuming a delayed appearance of RW by Δt (Iida et al, 1993), the following equation can be obtained:

$$A_w(t + \Delta t) = k(\alpha_1 \cdot A_t(t) \otimes \exp(-\beta_1 t) \\ + \alpha_2 \cdot A_t(t) \otimes \exp(-\beta_2 t)) \quad (2)$$

where $\otimes$ denotes the convolution integral and:

$$\alpha_{1,2} = \frac{a - 2c \pm \sqrt{a^2 - 4b}}{\pm 2\sqrt{a^2 - 4b}}, \quad \beta_{1,2} = \frac{a \pm \sqrt{a^2 - 4b}}{2},$$

$$a = k + k_w + k_w/p, \quad b = k \cdot k_w/p, \quad c = k_w/p, \quad p = k_w/k_2 \quad (3)$$

Following four approaches were performed to determine the rate constants and $A_w(t)$.

Approach by four parameters fitting: Four parameters, k, Δt, k_w, and p ($= k_w/k_2$), can be determined from the observed RW ($A_w(t)$) and the $A_t(t)$ curves by means of the nonlinear least square fitting (4PF approach).

Approach by one parameter fitting: Once three parameters, Δt, k_w, and p, are fixed by averaging values determined by the 4PF approach, k can then be determined by fitting the Equation 2 to measured $A_w(t)$ from $A_t(t)$ (1PF approach). In this procedure, single datum is sufficient, and thus k can be determined from $A_t(t)$ and the RW counts sampled at a single time point.

Approach from steady-state condition: Similarly to the 1PF procedures, k can be determined from the steady state condition, which is achieved by a continuous administration of $^{15}O_2$ as follows (SS approach). Incorporating the decay constant of ^{15}O ($\lambda = 0.00567$ per secs) into Equations 1a and 1b provides:

$$\frac{d}{dt}A^*_w(t) = k \cdot A^*_o(t) - k_w \cdot A^*_w(t) + k_2 \cdot C^*(t) - \lambda \\ \cdot A^*_w(t) \quad (4a)$$

$$\frac{d}{dt}C^*(t) = k_w \cdot A^*_w(t) - k_2 \cdot C^*(t) - \lambda \cdot C^*(t) \quad (4b)$$

where variables with the symbol * denote that no correction was made for the radioactivity decay of ^{15}O. After continuously administrating $^{15}O_2$, the radioactivity distribution of $A^*_o(t)$, $A^*_w(t)$, and $C^*_t(t)$ reaches a steady state. Thus, the following equations hold:

$$0 = k \cdot A^*_o(t) - k_w A^*_w(t) + k_2 C^*(t) - \lambda A^*_w(t) \quad (5a)$$

$$0 = k_w A^*_w(t) - k_2 C^*(t) - \lambda C^*(t) \quad (5b)$$

Given the values of k_w and k_2 which are determined as averages of 4PF, k can be calculated from the arterial $^{15}O_2$ and $H_2^{15}O$ concentrations at steady state as follows:

$$k = \lambda \left(\frac{k_w + k_2 + \lambda}{k_2 + \lambda}\right) \frac{A^*_w(t)}{A^*_o(t)} \quad (6)$$

Approach by the rate of whole body oxidative metabolism: In this study, an alternative approach is provided to obtain k, from the rate of oxidative metabolism in the whole-body system (BM approach). With this alternative approach, we assume that the production rate of RW or k is proportional to the rate of oxidative metabolism in the whole-body system (i.e., $BMRO_2$ (R_{O_2}, mL/min)). The rate of oxidative metabolism may change dependent on physiologic status of the subject. In addition, we assumed that this index can be defined from the difference of oxygen concentration between inhaled and exhaled trachea air samples. Therefore, the above can be expressed as follows:

$$k = c \cdot \frac{R_{O_2}}{V_{O_2}} \text{ (per min)} \quad (7a)$$

or

$$k_{BM} = \frac{k}{c} = \frac{R_{O_2}}{1.36 \cdot Hb \cdot V_{TB}} \quad (7b)$$

where c is the proportionality constant, k_{BM} the production rate of RW obtained from BM approach, V_{O_2} (mL) the total volume of molecular oxygen in total blood, 1.36 mL/g the amount of oxygen molecules combined with unit mass of hemoglobin, Hb (g/mL) represents the hemoglobin concentration in the arterial blood, and V_{TB} (mL) is the total volume of blood in the body.

Simulation

A series of simulation studies were performed to investigate the effects of errors on estimated $CMRO_2$ value in the model parameters (k, Δt, k_w, and p). In these simulations, a typical arterial blood time activity curve (TAC) of $^{15}O_2$ and $H_2^{15}O$ after DARG protocol (Kudomi et al, 2005) obtained in a monkey study was used. RW TACs were generated from the whole blood TAC by assuming baseline values of k as 0.13, 0.11, 0.34, and 0.73 per min, Δt as 20, 11, 5, and 3 secs, k_w as 0.38, 0.43, 0.98, and 0.87 per min, and p as 1.31, 1.01, 0.98, and 0.83, corresponding to humans, pigs, monkeys, and rats, respectively. Tissue TACs were generated by assuming $CBF = 50$ mL/min per 100 g and $OEF = 0.4$ ($CMRO_2$ was defined as: $CMRO_2 = CBF \times OEF \times C_aO_2$, where C_aO_2 is the arterial oxygen content. This simulation was intended to investigate magnitude of error as a percentage difference, so that arbitrary value of C_aO_2 was assumed) (Hayashi et al, 2003), using a kinetic formula for oxygen and water in the brain tissue (Mintun et al, 1984; Shidahara et al, 2002; Kudomi et al, 2005). $CMRO_2$ values were calculated by the DARG method (Kudomi et al, 2005), in which RW TACs were separated from the whole blood by changing k from 0.0 to 1.0 per min, Δt from 0 to 30 secs, k_w from 0.0 to 2.0 per min, and p from 0.0 to 2.0, respectively. Errors in the estimated $CMRO_2$ were presented as a percentage difference from the assumed true values.

Subjects

Subjects consisted of four groups including monkeys, pigs, rats, and clinical patients. Monkeys were six healthy *macaca fascicularis* with body weight of 5.2 ± 0.8 kg and age ranging from 3- to 4-year old. Pigs were three farm pigs

4

with body weight of 38 ± 9 kg and age from 4 to 12 months. Rats were 12 male Wistar rats with body weight of 300 ± 54 g and age from 7 to 8 weeks. All animals were studied during anesthesia. The animals were maintained and handled in accordance with guidelines for animal research on Human Care and Use of Laboratory Animals (Rockville, National Institute of Health/Office for Protection from Research Risks, 1996). The study protocol was approved by the Subcommittee for Laboratory Animal Welfare of National Cardiovascular Center.

Human data were retrospectively sampled from an existing database at National Cardiovascular Center which documented subjects who underwent PET examination after the ^{15}O-steady-state protocol. There were 231 total samples, with body weight and age ranging from 58 ± 10 kg, and 63 ± 14 years, respectively. Only the arterial $^{15}O_2$ and $H_2^{15}O$ radioactivity concentrations measured at the steady-state condition were used for the present analysis.

Experimental Protocol

The six monkeys were anesthetized using propofol (4 mg/kg/h) and vecuronium (0.05 mg/kg/h) assigned as a baseline in contrast to the after physiologically stimulated conditions. Animals were intubated and their respiration was controlled by an anesthetic ventilator (Cato, Drager, Germany). Each monkey inhaled 2,200 MBq $^{15}O_2$ for 20 secs. After 3 mins, the monkeys were injected with 370 MBq $H_2^{15}O$ for 30 secs by the anterior tibial vein. This was aimed at assessing both CBF and CMRO2 according to the DARG technique (Kudomi et al, 2005). At 30 secs before inhaling $^{15}O_2$ to the monkeys, arterial blood was withdrawn from the femoral artery for 420 secs at a rate of 0.45 mL/min using a Harvard pump (Harvard Apparatus, Holliston, MA, USA). The whole blood TAC was measured with a continuous monitoring system (Kudomi et al, 2003) and the $A_t(t)$ was obtained. Meanwhile, we also manually obtained 0.5 mL of arterial blood samples from the contralateral femoral artery at 30, 50, 70, 90, 110, 130, 160, 190, and 360 secs after the $^{15}O_2$ inhalation. For the analysis of sampled blood, 0.2 mL of the blood were used for measurement of the radioactivity concentration of the whole blood, and the rest of the blood sampled (~ 0.3 mL) was immediately centrifuged for separation to measure the plasma radioactivity concentration ($A_{plasma}(t)$, Bq/mL). The radioactivity concentration was measured using a well counter (Molecular Imaging Laboratory Co. Ltd, Suita, Japan).

In two monkeys, anesthetic level was changed by altering the injection dose of propofol from 4 (baseline) to 8 and then to 12 and 16 mg/kg/h in one monkey, and to 5 and then to 7, 10, and 15 mg/kg/h in the other. In another monkey, PaCO2 level was varied from 39 (baseline) to 47, and then to 33, 26, and 42 mm Hg by changing the respiratory rate. Each measurement for $^{15}O_2$ inhalation and $H_2^{15}O$ injection was initiated after at least 30 mins of applying the physiologic stimulation to achieve a steady state. All procedures were the same as those for the baseline, with the exception of the manual blood sample, which was obtained only once at 70 secs.

Before and after 6 mins of the $^{15}O_2$ inhalation, oxygen concentration in both inhaled (Fi_{O_2}, %) and end-tidal expiratory gas (Fe_{O_2}, %) was measured by the anesthetic ventilator in five out of the six monkeys. Using the respiration rate (r, per min) and the stroke volume (v, mL) indicated on the ventilator, the BMRO2 (R_{O_2} mL/min) was calculated using the following equation:

$$R_{O_2} = (Fi_{O_2} - Fe_{O_2}) \cdot v \cdot r.$$

All monkeys received a PET measurement to assess the CMRO2 at physiologically baseline condition. The scan protocol followed the DARG technique (Kudomi et al, 2005) in which a 6-mins single dynamic PET scan was performed in conjunction with the administration of dual tracers (i.e., $^{15}O_2$ followed by $H_2^{15}O$ after a 3-mins interval). PET scanner used was ECAT HR (Siemens-CTI, Knoxville, TN, USA), which provided 47 tomographic slice images for an axial field-of-view of approximately 150 mm. We performed arterial–sinus blood sampling to obtain a global OEF (OEF_{A-V}) (A–V difference approach). We sampled 0.2 mL of arterial and sinus blood simultaneously during each PET scan and measured their oxygen content (C_aO_2 and C_vO_2, respectively) (Kudomi et al, 2005). The OEF_{A-V} was calculated as: $OEF_{A-V} = (C_aO_2 - C_vO_2)/C_aO_2$.

With regards to the farm pigs involved in this experiment, we used existing data, which were originally obtained in one of the myocardial projects. During the study, three farm pigs were anesthetized. Anesthesia was induced by ketamine (10 mg/kg) and maintained using propofol (4 mg/kg/h). Animals were intubated and their respiration was controlled by the anesthetic ventilator. Venous blood was labeled with $^{15}O_2$ using a small artificial lung unit (Magata et al, 2003). $^{15}O_2$-labeled blood (222 to 700 MBq) was injected for 10 secs via anterior tibial vein. At 30 secs before this injection, arterial blood was withdrawn from the femoral artery at a rate of 0.45 mL/min using the Harvard pump and continued for 420 secs. The whole blood TAC ($A_t(t)$) was then measured with a continuous monitoring system (Kudomi et al, 2003). Meanwhile, we manually sampled 0.5 mL of arterial blood from the contralateral femoral artery at 30, 60, 90, 90, 120, 180, 240, and 300 secs after the $^{15}O_2$-labeled blood injection. For the analysis of sampled blood, 0.2 mL of the blood were used for measurement of the radioactivity concentration of the whole blood, and the rest of the blood sampled (~ 0.3 mL) was immediately centrifuged for separation to measure the plasma radioactivity ($A_{plasma}(t)$, Bq/mL). The radioactivity was measured using the well counter.

Data for rats were also originally obtained for other projects, and only the blood counts were used in this study. Anesthesia was induced with pentobarbital (50 mg/kg). A 10 mL of venous blood was labeled $^{15}O_2$ using a small artificial lung unit as described previously (Magata et al, 2003), and approximately 1 mL of $^{15}O_2$-labeled blood (37 to 74 MBq) was injected for 30 secs via the tail vein. Arterial blood samples of 0.1 mL each were obtained from the femoral artery at 5-secs intervals for 60 secs and 10-secs intervals for another 60 secs after the injection. Whole blood radioactivity concentration was measured using the well counter to be used as $A_t(t)$. Arterial blood samples of

0.2 mL each were obtained at 30, 60, 90, and 120 secs, and the plasma radioactivity concentration $(A_{plasma}(t))$ was measured by the well counter.

For clinical patients, the blood radioactivity concentration was obtained from previously performed PET examinations, which followed the steady-state protocol (Hirano *et al*, 1994). Each patient inhaled both $^{15}O_2$ and $C^{15}O_2$ to reach the steady state with an inhalation dose of approximately 1,200 and 500 MBq/min, respectively. Five to seven arterial blood samples were obtained during the steady state from the brachial artery. Mean values of radioactivity concentration of the whole blood and plasma, $A_t(t)$ and $A_{plasma}(t)$, respectively, were obtained for both $^{15}O_2$ and $C^{15}O_2$ PET examination.

Data Analysis

Using the blood activity data obtained from monkeys, pigs, and rats at baseline conditions, k as well as Δt, k_w and p were first determined by the 4PF approach, in which Equation 2 was applied to fit the $A_w(t)$ using the observed $A_t(t)$. Because the solubility of the oxygen is negligibly small in the plasma, we assumed that all radioactivity in plasma fraction comes from $H_2^{15}O$ and that the water content ratio of whole blood to plasma (R) does not change during measurement, which means that the kinetics of water molecules immediately reach equilibrium between the plasma and the cellular fraction (Mintun *et al*, 1984; Iida *et al*, 1993). Thus, $A_w(t)$ was obtained from the equation: $A_w(t) = A_{plasma}(t) \cdot R$, where R value was obtained from the sampled blood at the end of the scan (at which all the radioactivity in the blood can be considered as coming from $H_2^{15}O$ because inhaled $^{15}O_2$ is all metabolized).

Given that the values of Δt, k_w, and p were averages determined from 4PF for monkeys, pigs, and rats, only k was determined by fitting Equation 2 to A_w. This was calculated at various points in time, more specifically, in 30, 50, 70, 90, 110, 130, 160, and 190 secs for monkeys, in 30, 60, 90, 90, 120, 180, and 240 secs for pigs, and in 30, 60, 90, and 120 secs for rats. The optimal time point for k under the 1PF approach was determined, so that $(k_{4PF} - k_{1PF})/k_{4PF}$ reaches a minimal value. Here, k_{4PF} and k_{1PF} denote k values determined by the 4PF and 1PF approaches, respectively. The values of k in monkeys at baseline condition, together with those in pigs and rats were compared between 4PF and 1PF approaches, in which a k value from the optimal single time point was used.

In three of the monkeys, which were physiologically stimulated, k of 1PF approach was obtained using single time point of A_w. Assuming the total blood volume (V_{TB}) for monkeys as 360 mL (Lindstedt and Schaeffer, 2002), and using Hb as measured value in each experiment, k_{BM} was calculated from R_{O_2} according to Equation 7b. Then, k_{BM} obtained as: $k_{BM} = 0.00204R_{O_2}$ was compared with k determined by 1PF.

For clinical data obtained from the steady-state (SS approach) PET examinations, Equation 6 was used to determine the k values of the SS approach for each patient, in which values of k_w and k_2 were 0.38 and 0.29 per min as obtained in a previous work by Huang *et al* (1991).

$CMRO_2$ and OEF values in monkeys at baseline condition were calculated using the RW TACs obtained by four different methods (i.e., directly measured $A_w(t)$ $(n = 6)$, 4PF $(n = 6)$, 1PF $(n = 6)$, and BM approaches $(n = 5)$). Regions-of-interest were selected for over the whole brain, and $CMRO_2$ and OEF values were obtained in those regions-of-interest. The $CMRO_2$ values compared among the four methods mentioned above to estimate RW TACs. The Bland–Altman method was applied to analyze the agreement of OEF values between the methods. Also, OEF values were compared with OEF_{A-v}.

All data were presented as mean ± 1 standard deviation. Student's *t*-test was used and Pearson's regression analysis was applied to compare two variables. A probability value of < 0.05 was considered statistically significant.

Results

Figure 1 shows results from the simulation study, and shows the magnitude of errors in $CMRO_2$ calculated by the DARG method as well as errors in the parameters, k, Δt, k_w, and p. Errors in $CMRO_2$ were most sensitive to errors in k amongst all species, namely the production rate constant of RW in the arterial blood. After errors in k, errors in $CMRO_2$ were sensitive to errors in Δt. Errors in k_w and p, however, appeared to cause relatively insignificant errors in $CMRO_2$. More specifically, only 5 to 10% errors are caused in $CMRO_2$ by a change of ± 50% in k_w and p.

Figures 2A–2C show examples of the arterial whole blood curves (A_t) and RW TAC (A_w) observed in typical studies on a monkey, a pig, and a rat, respectively. The RW curves became constant after a period in all species. The rise time or appearance of the RW curves, $A_w(t)$, was significantly delayed compare to that of whole blood curve, $A_t(t)$. $A_w(t)$ curves fitted by 4PF well reproduced the measured RW curves in three species: monkeys, pigs, and rats. Table 2 summarizes values of k, Δt, k_w, and p obtained by the four parameter fitting (4PF approach), at the baseline for monkeys, pigs, and rats, and also k value obtained by the steady-state formula for clinical patients. Those comparisons showed that the k was significantly different among species $(P < 0.001)$ except between pig and human subjects, and it was significantly lower in smaller animals. Likewise, Δt showed significant differences among the three species $(P < 0.001)$, and it was also lower in smaller animals.

Table 3 summarizes k and $CMRO_2$ values obtained from a series of PET experiments performed on six monkeys at baseline condition, and for increased anesthesia (in two monkeys), and changed $PaCO_2$ levels (in one monkey). The best agreement of k values between 4PF and 1PF approaches was obtained from the blood sample data taken at 60, 70, and 60 secs in pigs, monkeys, and rats, respectively, and was used in the 1PF approach. With this
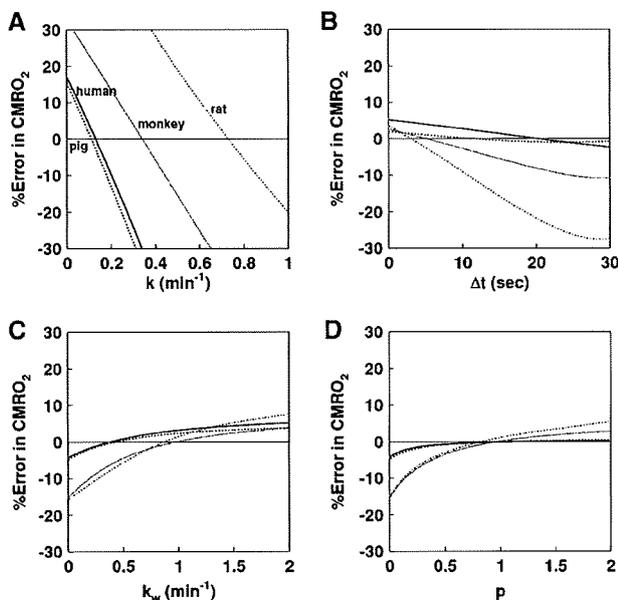
6

Figure 1 Error in $CMRO_2$ values due to errors in (A) k, (B) Δt, (C) k_w, and (D) p for assumed human, pig, monkey and rat. The same type of line indicates the same species. The percentage differences in the $CMRO_2$ values from the assumed true values (Table 1) were plotted as a function of the simulated value of k, Δt, k_w, and p.
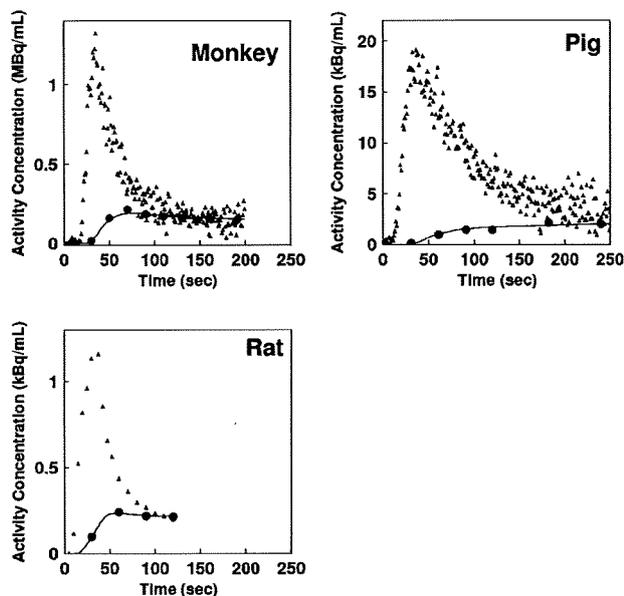

Figure 2 Representative comparison of the measured arterial whole blood and RW time activity curves for monkey, pig, and rat. Closed triangles and closed circles represent the measured whole blood and RW time activity curves, respectively. Estimated time activity curves by 4PF approach were also plotted in a solid line, and indicated a good agreement with the measured one.

optimized calibration protocol, k values were in a good agreement between 4PF and 1PF approaches. As shown in Figure 3, the regression analysis

showed significant correlation for 21 animals including 6 monkeys, 3 pigs, and 12 rats ($P < 0.001$), and there was no significant difference between the two variables. Figure 4 shows that k values calculated by the 1PF approach (at an optimized time) were in a good agreement with those calculated with the $BMRO_2$. Namely, the regression analysis showed significant correlation ($P < 0.001$, $n = 16$) and also that there was no significant difference between the two variables. Note that, in the $CMRO_2$ calculation by $BMRO_2$, k values were normalized according to the regression line shown in Figure 4. It should also be noted that calculated $CMRO_2$ values at the baseline shown in Table 3 were not significantly different among the four techniques. The average ($\pm$ s.d.) values of obtained OEF were 0.53 ± 0.08, 0.52 ± 0.09, 0.54 ± 0.08, 0.54 ± 0.09, and 0.56 ± 0.04 from A–V difference, directly RW measured approach, 4PF, 1PF, and BM approaches, respectively. The Bland–Altman analysis of OEF values between from A–V difference and from others showed small over/underestimation, that is., with bias $\pm$ s.d. of -0.02 ± 0.09, 0.01 ± 0.07, 0.01 ± 0.08, and 0.02 ± 0.09, by direct RW, 4PF, 1PF, and BM approaches, respectively. Neither of the current methods (direct RW, 4PF, 1PF, and BM) was significantly different from A–V difference approach.

Discussion

Our study showed that the mathematical formula based on the physiologic model that reproduced the time-dependent concentration of RW in the arterial blood after a short-period inhalation of $^{15}O_2$ is indeed adequate. Our approach also simplified the procedures for sequential assessment of RW in $^{15}O_2$ inhalation PET studies, although previous approaches required frequent blood samples and centrifuges of each arterial blood sample. The present approach is an extension of a previous study by Iida et al (1993) and Huang et al (1991). It is essential if one intends to apply the rapid $^{15}O_2$ PET technique (Kudomi et al, 2005) to pharmacologic and physiologic stress studies on a wide range of species. Because the PET acquisition period can be prolonged > 3 mins, statistical accuracy can be significantly improved as compared with Ohta et al (1992) and other researchers (Fujita et al, 1999; Vafaee and Gjedde, 2000; Okazawa et al, 2001a, b; Yamauchi et al, 2003; Mintun et al, 2002), under which to avoid effects of RW, the data acquisition period was limited only to < 3 mins (Meyer et al, 1987; Ohta et al, 1992).

The present RW formula consists of three rate parameters of the production rate of RW in the arterial blood (k), and the forward and backward diffusion rate constants of RW between the blood and the peripheral tissues. The k was presumed to correspond to the oxygen metabolism in the total body system, $BMRO_2$, and was in fact shown to be

Table 2 Averaged values of k, Δt, k_w, and p for monkeys, pigs, rat, and human subjects under baseline condition

	Weight (kg)	k (per min)	Δt (secs)	k_w (per min)	p
Monkey	5.2 ± 0.8^a	0.34 ± 0.16^a	4.5 ± 1.4^a	0.98 ± 0.48	0.98 ± 0.30
Pig	38 ± 9^a	$0.11 \pm 0.02^{a,b}$	10.8 ± 1.8^a	0.83 ± 0.19	1.01 ± 0.26
Rat	0.30 ± 0.054^a	0.73 ± 0.16^a	2.9 ± 1.7^a	0.87 ± 0.30	0.83 ± 0.32
Human	58 ± 10^a	$0.129 \pm 0.023^{a,b}$	—	—	—

Monkey: $n = 6$; pig: $n = 3$; rat: $n = 12$; and human: $n = 231$. Measured values were obtained by 4PF for monkey, pig, rats, whereas those for human were obtained using data in a steady-state method.
[a]Denotes $P < 0.001$ for other species.
[b]Denotes that the difference was not significant in k between pig and human subjects.

Table 3 Values of k and $CMRO_2$ in the whole brain region for monkeys under physiologically baseline and stimulated conditions

ID	Condition	k (per min)			$CMRO_2$ (mL/min per 100 g)			
		4PF	1PF	$BMRO_2$	Reference	4PF	1PF	$BMRO_2$
1	BL	0.36	0.42	—	3.7	3.7	3.6	—
2	BL	0.62	0.66	1.24	3.0	3.3	3.4	3.4
3	BL	0.32	0.39	0.83	3.0	3.1	3.0	2.9
	(Dose of propofol)							
4	BL	0.21	0.18	0.55	2.0	2.0	2.0	1.8
	8 mg/kg/h	—	0.30	0.69	—	—	—	—
	12 mg/kg/h	—	0.23	0.52	—	—	—	—
	16 mg/kg/h	—	0.16	0.40	—	—	—	—
5	BL	0.12	0.15	0.31	2.1	2.1	2.0	1.8
	5 mg/kg/h	—	0.15	0.32	—	—	—	—
	7 mg/kg/h	—	0.16	0.35	—	—	—	—
	10 mg/kg/h	—	0.18	0.36	—	—	—	—
	15 mg/kg/h	—	0.071	0.29	—	—	—	—
	($PaCO_2$ level)							
6	BL	0.43	0.46	0.95	2.8	3.1	3.0	3.3
	47 mm Hg	—	0.20	0.64	—	—	—	—
	33 mm Hg	—	0.21	0.46	—	—	—	—
	26 mm Hg	—	0.14	0.28	—	—	—	—
	42 mm Hg	—	0.33	0.82	—	—	—	—

4PF, four parameters fitting; 1PF, one parameter fitting; $BMRO_2$, total body metabolic rate of oxygen; BL, baseline condition.
Reference: RW TAC was obtained using measured RW data at a baseline condition in all monkeys ($n = 6$). No statistically significant differences were found in $CMRO_2$ between reference and other techniques.
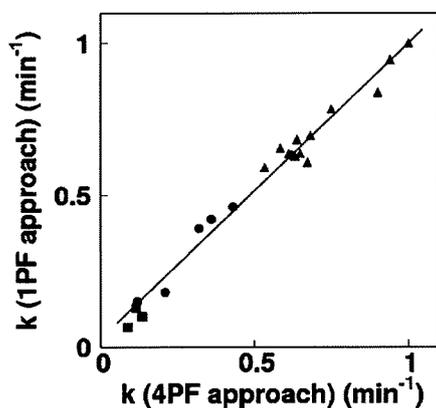

Figure 3 Comparison of the production rates of RW (k, per min) obtained by 4PF and those by 1PF. Squares, circles, and triangles correspond to pigs, monkeys, and rats, respectively. The regression line was $y = 0.97x + 0.026$ (per min) ($r = 0.98$).
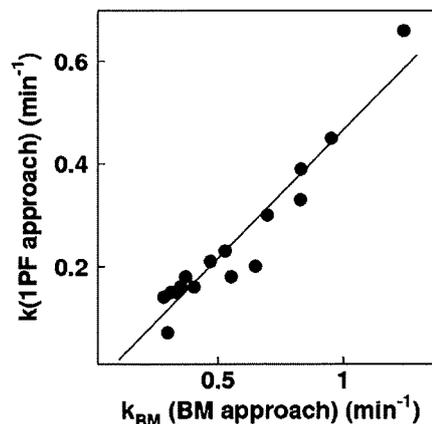

Figure 4 Comparison of the production rates of RW obtained by BM approach and those by 1PF approach in five monkeys at various anesthetic and $PaCO_2$ levels. The regression line was $y = 0.50x - 0.034$ (per min) ($r = 0.95$).

8

significantly correlated to BMRO$_2$, as measured from the trachea gas sampling (Figure 4). The latter two parameters (k_w and p) appeared to be consistent and did not differ across various species (Table 2). Also, change in those parameters was less sensitive in CMRO$_2$ (Figure 1). These findings suggest that the production of RW after inhalation of $^{15}O_2$ could be described only by a single parameter of k, as shown in Figure 3, although further studies are required to validate this because the method was only tested in a group with small number of subjects of particular physiologic situation (under anesthesia) and has not been applied to different populations. It is also important to note that this parameter (k) estimated from the BMRO$_2$ (i.e., BM approach) provided CMRO$_2$, which was consistent with the trachea gas samplings shown in Figure 4, and that the obtained OEF values by the approaches of 4PF, 1PF, and BM applied in the present study were not significantly different to that by A–V difference approach as revealed by Bland–Altman analysis.

The simulation study also showed that the most sensitive parameter in CMRO$_2$ was the RW production rate constant, k, followed by Δt. It was therefore suggested that k could be determined with a single blood sampling procedure using the 1PF approach, in which other parameter values were determined and fixed from results from the 4PF approach. It was further showed that k could be obtained from the BM approach as determined from oxygen concentration in the expiration gas. Both 1PF and BM approaches appeared to be robustly useful in $^{15}O_2$ PET for assessing quantitative CMRO$_2$ and CBF in clinical studies.

It is important to note that k varies significantly depending on the physiologic status even in the same species, as seen in Figure 4. According to the simulation study in Figure 1, this variation causes nonnegligible errors in CMRO$_2$, if a constant k is used. Changes in k from 0.1 to 0.6 per min causes errors in CMRO$_2$ of $\pm 30\%$ in anesthetized monkeys. Results from clinical studies, however, showed the variation in k being less. As shown in Table 2, k for clinical patients was 0.129 ± 0.023 per min, and the coefficient of variation was approximately 18%. Previous work by Huang et al (1991) also showed similar value with comparable variations, namely 0.131 ± 0.026 per min in six human subjects. These variations caused only $\pm 5\%$ errors in CMRO$_2$, according to the simulation shown in Figure 1. The small variation in k in clinical patients is attributed to the fact that all subjects were studied at a relatively stable condition without physiologic stimulation. However, careful attention is needed if one intends to scan the patients whose whole-body oxygen metabolism is largely changed from the baseline condition. For example, during several pharmacologically stressed (Wessen et al, 1997; Kaisti et al, 2003), exercise-induced physically stressed, and hyper- or hypothermia (Sakoh and Gjedde, 2003) conditions.

The simulation also showed that size of errors in CMRO$_2$ increased in smaller animals, where the value of k was larger. Recently, CMRO$_2$ as well as CBF have been measured in rats using a small animal PET scanner (Magata et al, 2003; Yee et al, 2006). Magata et al performed multiple blood samplings and plasma separation for multiple blood samples to estimate the RW in their experiment involving rats. The procedures were crucial, but have caused serious alterations of physiologic condition in heart pressure and heart rate due to large amount of blood samples for small animals. Our proposed simplified technique for estimating RW from a single blood sample or from BMRO$_2$, is essential for small animals to be able to maintain the physiologic status. The calculation of CMRO$_2$ also requires whole blood arterial TAC, which can be obtained from arterial blood samplings and could change the physiologic condition. However, such blood sampling could also be avoided by an arterial–venous bypass (Weber et al, 2002; Laforest et al, 2005), by placing a probe in femoral artery (Pain et al, 2004), or by a noninvasive method (Yee et al, 2006).

Mintun et al (1984) has proposed a simple procedure for RW correction based on a linear interpolation for the bolus $^{15}O_2$ inhalation 60-secs PET scan. As shown in Figure 2, the RW curve is not linear particularly in smaller animals, and a systematic error may be caused or scan duration is limited. Ohta et al (1992) and other investigators (Ohta et al, 1992; Fujita et al, 1999; Vafaee and Gjedde, 2000; Okazawa et al, 2001a, b; Yamauchi et al, 2003; Mintun et al, 2002), however, have used a technique which does not take into account the RW contribution. Only initial short-period data, namely the 3 mins after the bolus inhalation of $^{15}O_2$, were used in their approach, and thus estimated parameters suffered from statistical uncertainties. The present methodology to estimate RW in the arterial blood allows the prolongation of a PET acquisition period. The technique can also be applicable to the recently proposed sequential administration protocol of $^{15}O_2$ followed by $H_2^{15}O$ to estimate CMRO$_2$ and CBF simultaneously from a single session of a PET scan (Kudomi et al, 2005). This protocol, however, required a separation of a RW TAC from the whole blood TAC as showed recently (Kudomi et al, 2007).

The k_{BM} determined from the total body oxygen metabolism, namely the BM approach, was significantly greater than k obtained by the 4PF or the 1PF approach, by a factor 2, as shown in Figure 4. The reason is not clear, but partly attributed to the limitation of the simplified model. The body system consists of various organs which have different oxygen metabolism along with different circulation systems and with transit times. It is well known that the apparent rate constant defined with a simplified compartmental model could be underestimated as compared with an average of true rate constants, known as heterogeneity effects (Iida et al, 1989; Aston et al, 2002). This is, however, not essential.

167